

TOPICAL REVIEW

The ionic conductivity in lithium-boron oxide materials and its relation to structural, electronic and defect properties: insights from theory

To cite this article: Mazharul M Islam *et al* 2012 *J. Phys.: Condens. Matter* **24** 203201

View the [article online](#) for updates and enhancements.

Related content

- [Topical Review](#)
Paul Heitjans and Sylvio Indris
- [Double perovskites with ferromagnetism above room temperature](#)
D Serrate, J M De Teresa and M R Ibarra
- [How chemistry controls electron localization in 3d1 perovskites: a Wannier-function study](#)
E Pavarini, A Yamasaki, J Nuss *et al*.

Recent citations

- [Some device implications of voltage controlled magnetic anisotropy in Co/Gd 2 O 3 thin films through REDOX chemistry](#)
Guanhua Hao *et al*
- [Lithium Diffusion Mechanisms in -LiMO₂ \(M = Al, Ga\): A Combined Experimental and Theoretical Study](#)
Mazharul M. Islam *et al*
- [First-principles study of structural, electronic, energetic and optical properties of substitutional Cu defect in Li 2 B 4 O 7 scintillator](#)
C. Santos *et al*

TOPICAL REVIEW

The ionic conductivity in lithium-boron oxide materials and its relation to structural, electronic and defect properties: insights from theory

Mazharul M Islam^{1,2}, Thomas Bredow^{1,2} and Paul Heitjans^{2,3}

¹ Mulliken Center for Theoretical Chemistry, Universität Bonn, Beringstraße 4–6, 53115 Bonn, Germany

² ZFM—Zentrum für Festkörperchemie und Neue Materialien, Leibniz Universität Hannover, Callinstrasse 3a, 30167 Hannover, Germany

³ Institut für Physikalische Chemie und Elektrochemie, Leibniz-Universität Hannover, Callinstrasse 3-3a, 30167 Hannover, Germany

E-mail: rana-islam@xtch.uni-bonn.de, bredow@thch.uni-bonn.de and heitjans@pci.uni-hannover.de

Received 4 October 2011

Published 27 April 2012

Online at stacks.iop.org/JPhysCM/24/203201

Abstract

We review recent theoretical studies on ion diffusion in $(\text{Li}_2\text{O})_x(\text{B}_2\text{O}_3)_{1-x}$ compounds and at the interfaces of $\text{Li}_2\text{O}:\text{B}_2\text{O}_3$ nanocomposite. The investigations were performed theoretically using DFT and HF/DFT hybrid methods with VASP and CRYSTAL codes. For the pure compound B_2O_3 , it was theoretically confirmed that the low-pressure phase B_2O_3 -I has space group $P3_121$. For the first time, the structure, stability and electronic properties of various low-index surfaces of trigonal B_2O_3 -I were investigated at the same theoretical level. The (101) surface is the most stable among the considered surfaces. Ionic conductivity was investigated systematically in Li_2O , LiBO_2 , and $\text{Li}_2\text{B}_4\text{O}_7$ solids and in $\text{Li}_2\text{O}:\text{B}_2\text{O}_3$ nanocomposites by calculating the activation energy (E_A) for cation diffusion. The Li^+ ion migrates in an almost straight line in Li_2O bulk whereas it moves in a zig-zag pathway along a direction parallel to the surface plane in Li_2O surfaces. For LiBO_2 , the migration along the c direction ($E_A = 0.55$ eV) is slightly less preferable than that in the xy plane ($E_A = 0.43$ – 0.54 eV). In $\text{Li}_2\text{B}_4\text{O}_7$, the Li^+ ion migrates through the large triangular faces of the two nearest oxygen five-vertex polyhedra facing each other where E_A is in the range of 0.27–0.37 eV. A two-dimensional model system of the $\text{Li}_2\text{O}:\text{B}_2\text{O}_3$ interface region was created by the combination of supercells of the Li_2O (111) surface and the B_2O_3 (001) surface. It was found that the interface region of the $\text{Li}_2\text{O}:\text{B}_2\text{O}_3$ nanocomposite is more defective than Li_2O bulk, which facilitates the conductivity in this region. In addition, the activation energy (E_A) for local hopping processes is smaller in the $\text{Li}_2\text{O}:\text{B}_2\text{O}_3$ nanocomposite compared to the Li_2O bulk. This confirms that the $\text{Li}_2\text{O}:\text{B}_2\text{O}_3$ nanocomposite shows enhanced conductivity along the phase boundary compared to that in the nanocrystalline Li_2O .

(Some figures may appear in colour only in the online journal)

Contents

1. Introduction	4. Bulk properties	4
2. General overview	4.1. Lithium oxide (Li_2O)	4
3. Computational methods	4.2. Boron oxide (B_2O_3)	5
	4.3. $\text{Li}_2\text{O}-\text{B}_2\text{O}_3$ mixed compounds	7
	5. Surface properties	8

5.1. Surfaces of Li_2O	8
5.2. Surfaces of B_2O_3	9
6. Defects and diffusion in Li_2O	10
6.1. Li_2O bulk	10
6.2. Li_2O surfaces	12
7. Defects and diffusion in LiBO_2 bulk	15
7.1. Cation vacancy in LiBO_2	15
7.2. Electronic properties	15
7.3. Migration of a Li^+ ion	16
8. Defects and diffusion in $\text{Li}_2\text{B}_4\text{O}_7$ bulk	17
8.1. Cation vacancy in lithium tetraborate	18
8.2. Migration of a Li^+ ion	20
9. Defects and diffusion in $\text{Li}_2\text{O}:\text{B}_2\text{O}_3$ nanocomposites	21
9.1. Structural models	22
9.2. Defects	23
9.3. Li migration	24
10. Summary and conclusions	25
Acknowledgments	27
References	27

1. Introduction

In recent years, ceramic oxides have attracted considerable attention due to their broad potential applications as advanced materials with controlled chemical, mechanical, electrical, magnetic, and optical properties (see [1] and references therein). Many of these properties are attributed to the mobility of metal ions. A metal ion can migrate from a regular site to an interstitial site or to an adjacent vacant lattice site. An important criterion for the probability of these processes is the corresponding activation energy. Sometimes, it is difficult to accurately determine this quantity with experimental techniques. Quantum-chemical approaches can be utilized to calculate the activation energy for the elementary steps.

Ion conductivity in ceramic oxides has been observed in single-phase systems as well as in composites of different components [1–7]. A good example of a single-phase nanocrystalline ceramic as a Li ion conductor is Li_2O [2]. Nanocomposite materials often show enhanced conductivity compared to the single-phase ceramic oxides which is attractive with respect to possible applications in battery systems, fuel cells or sensors. For example, the conductivities in $\text{Li}_2\text{O}:\text{B}_2\text{O}_3$ [1–3] and $\text{Li}_2\text{O}:\text{Al}_2\text{O}_3$ nanocomposites [6] are higher than in nanocrystalline Li_2O , although B_2O_3 and Al_2O_3 are insulators.

This surprising effect was attributed to the increased fraction of structurally disordered interfacial regions and the enhanced surface area of the nanosize particles (figure 1 [1]). For the nanocrystalline samples, the relative volume fraction of the interface becomes close to the percolative pathways. In this case, the highly conducting interface region can act as a bridge between two Li_2O grains not in direct contact with each other, opening up additional paths for Li ions.

In contrast, the corresponding microcrystalline composites do not show enhanced diffusivity [2, 3, 6]. For microcrystalline samples, the interface region between B_2O_3

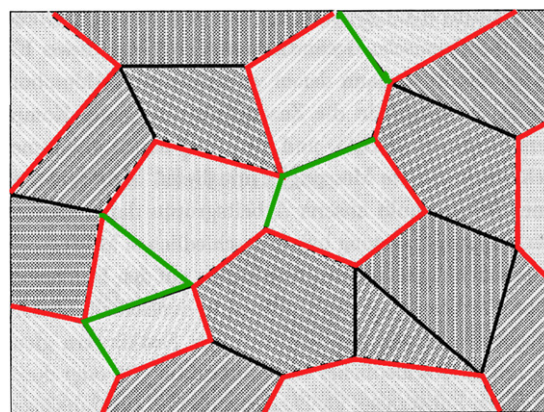


Figure 1. Sketch of $\text{Li}_2\text{O}:\text{B}_2\text{O}_3$ composite material; light grey areas represent ionic conductor grains (Li_2O) and dark grey areas represent insulator grains (B_2O_3). The network of interfaces consists of interfaces between ionic conductor grains (green lines), interfaces between insulator grains (black lines) and interfaces between ionic conductor and insulator grains (red lines) [1].

and Li_2O grains does not play a significant role since its width is negligible compared to the grain sizes, and conducting paths can open up only when two Li_2O grains come into direct contact with each other.

In this context, the expression ‘interface’ denotes the two-dimensional transition region between three-dimensional regions that are homogeneous in the equilibrium case [8]. In nanocrystalline Li_2O , there are interfaces between similar crystallites whereas $\text{Li}_2\text{O}:\text{B}_2\text{O}_3$ nanocomposites contain three types of interface: between the ionic conductor grains, between the insulator grains and between the ionic conductor and the insulator grains (see figure 1).

In a previous theoretical study, we have developed atomistic models of the $\text{Li}_2\text{O}:\text{B}_2\text{O}_3$ nanocomposite based on periodic slabs [9]. Investigations were performed to clarify whether the observed enhancement of Li conductivity in the $\text{Li}_2\text{O}:\text{B}_2\text{O}_3$ interface is due to a higher defect concentration (thermodynamically controlled) or to smaller activation barriers for local hopping processes (kinetically controlled). This is a general question for all nanocrystalline materials. These models allow a direct simulation of the defect formation and mobility at atomic scale without any experimental input. They can give insight into the local bonding situation at the interface which is difficult to obtain from experiments.

In several preliminary studies, calculated bulk properties of Li_2O [10], B_2O_3 [11], LiBO_2 [12, 13] and $\text{Li}_2\text{B}_4\text{O}_7$ [13, 14] were compared with available experimental data as critical tests for models and methods. In order to predict the most stable surface planes, the surface properties of Li_2O [15] and B_2O_3 [16] were also investigated. Finally, defects and diffusion in bulk [10] and surfaces [15] of Li_2O , and in crystalline LiBO_2 [12] and $\text{Li}_2\text{B}_4\text{O}_7$ [17], and at the interfaces of $\text{Li}_2\text{O}:\text{B}_2\text{O}_3$ nanocomposite [9] were investigated and compared with available experimental data.

This review is organized as follows. In section 2 we give a general overview of recent investigations on $\text{Li}_2\text{O}-\text{B}_2\text{O}_3$ materials. Section 3 contains a brief description of computational methods that we have used in our studies.

Our results are discussed in sections 4–7. Finally, we provide a summary in section 8.

2. General overview

Lithium oxide has become a subject of considerable interest because of its potential applications. It is used in high-capacity energy storage devices for next-generation electric vehicles, in lightweight high-power-density lithium ion batteries for heart pacemakers, mobile phones and laptop computers [18, 19], and as blanket breeding material for deuterium–tritium fusion reactors [20]. Diffusion and ionic conduction in Li_2O are subjects of great interest due to the superionic behaviour of this material. Both theoretical and experimental investigations have been performed for Li_2O on the energetic [21–23], electronic [23–32], and defect properties [29–42], and the ion conduction mechanism [1–3, 34, 35, 43–47].

The dominant intrinsic defects in Li_2O are point defects [33–35], either as cation vacancies or of cation Frenkel type, i.e., vacancies and interstitials in the Li sublattice. Schottky disorder is also observed, but it is not as predominant as the cation Frenkel defect [34]. On the other hand, the dominant irradiation defects in Li_2O are known as F centres [29, 36, 37] and F^+ centres [29–31, 38, 41, 42]. In a combined experimental and theoretical study of defects in Li_2O , Chadwick *et al* [34] showed that Li^+ ions migrate via cation vacancies. In this study, a combination of ac conductivity measurements and non-linear least-squares computer simulation was performed, where the activation energy for Li^+ diffusion (E_A) was investigated. Chadwick *et al* [34] reported an experimental value of 0.49 eV for the activation energy E_A whereas their calculated value was only 0.21 eV. In more recent theoretical investigations [35, 43, 44] where density-functional methods based on the local density approximation (LDA) were employed, it was also observed that Li^+ ions are migrating through the cation vacancies. For this process, activation energies of 0.34 eV [35], 0.30 eV [43] and 0.29 eV [44] were calculated. As pointed out in, e.g., [1], two types of experimental approach are employed for the study of diffusion and ionic conduction in nanocrystalline ceramics. The tracer diffusion method is a macroscopic method while NMR relaxation is known as a microscopic method. The value of E_A for Li ion diffusion in Li_2O derived basically from the NMR relaxation method is 0.31 eV, whereas 0.95 eV is obtained with the tracer diffusion method. The NMR relaxation method gives a smaller E_A compared to the tracer diffusion method because it is sensitive to short-range motions of the ions. The barrier heights correspond to a single jump process. On the other hand, the tracer diffusion method probes the long-range transport [1].

B_2O_3 plays an important role in modern ceramic and glass technology [1, 2, 48]. Two polymorphs exist [49–51] where the boron atoms have different coordination numbers. At normal pressure, B_2O_3 has a trigonal structure (B_2O_3 –I) characterized by a three-dimensional network of corner-linked BO_3 triangles [49, 50]. An orthorhombic modification (B_2O_3 –II) exists at high pressures, consisting of a framework

of linked BO_4 tetrahedra [51]. Some controversy exists in the literature regarding the space group classification of B_2O_3 –I. Effenberger *et al* [49], based on a refinement of previously published x-ray data [50], concluded that the B_2O_3 –I structure belongs to space group (152) $P3_121$, instead of (144) $P3_1$ as suggested earlier [50].

The experimental lattice parameters [49, 50] of trigonal B_2O_3 –I are $a = 4.3358 \text{ \AA}$, $c = 8.3397 \text{ \AA}$ and $\gamma = 120^\circ$. The experimental value of the heat of atomization is 3127 kJ mol^{-1} [52]. Several experimental [53, 54] and theoretical investigations [55, 56] have been performed for the electronic structure of B_2O_3 –I. However, no experimental value for the bandgap is available in the literature. Li *et al* [55] found a bandgap of 6.2 eV, based on density-functional theory (DFT) calculations using the local density approximation (LDA).

Up to now, nine lithium borate compounds have been reported in the Li_2O – B_2O_3 phase diagram, namely Li_3BO_3 , α - $\text{Li}_4\text{B}_2\text{O}_5$, β - $\text{Li}_4\text{B}_2\text{O}_5$, $\text{Li}_6\text{B}_4\text{O}_9$, LiBO_2 , $\text{Li}_2\text{B}_4\text{O}_7$, $\text{Li}_3\text{B}_7\text{O}_{12}$, LiB_3O_5 and $\text{Li}_2\text{B}_8\text{O}_{13}$ [57–60]. Only Li_3BO_3 (lithium orthoborate), $\text{Li}_6\text{B}_4\text{O}_9$, LiBO_2 (lithium metaborate), $\text{Li}_2\text{B}_4\text{O}_7$ (lithium tetraborate) and LiB_3O_5 (lithium triborate) are stable under ambient conditions. A common feature of all anhydrous lithium borate crystalline structures is the boron–oxygen anion subsystem. This subsystem is capable of producing a covalent anion framework with the help of two stable oxygen coordinations of boron atoms— BO_3 -triangles and BO_4 -tetrahedrons that have a polycondensation susceptibility [61]. Lithium ions, in turn, are coupled with the anion subsystem by an ionic bond that may result in the appearance of ionic conductivity and of superionic properties.

Single crystals of the Li_2O – B_2O_3 system are of considerable interest for their practical applications. Due to its good dissolvability, low melting temperature and resistance against transition metal contamination, lithium metaborate (LMB) LiBO_2 is widely employed as a flux or solvent [62]. It is an excellent basic flux for silicate analysis [63], for the synthesis of low-density γ - Al_2O_3 from high-density α - Al_2O_3 [64], for the identification and characterization of resistant minerals containing uranium and thorium [65] and for the growth of single crystals [66–68]. LMB is also used as a chemical modifier during mechano-chemical synthesis processes for generating new compounds from clays and refractory materials [69]. Because of its deep-ultraviolet transparency combined with mechanical durability and high optical damage thresholds [70, 71], LMB is one of the most attractive materials for wide bandgap non-linear optics. Recent experimental studies [72, 73] show that LiBO_2 is a good ion conductor.

Hydrogen is undeniably an appropriate candidate to overcome key challenges associated with future green energy sources [74, 75]. A recent study [76] shows that lithium borohydride is an attractive potential hydrogen storage material whose dehydration reaction forms LiBO_2 along with two molecules of water.

Crystalline lithium tetraborate (LTB) $\text{Li}_2\text{B}_4\text{O}_7$ has lots of important physical properties, such as high coefficient of electrochemical coupling, low velocity of propagation of

surface acoustic waves, zero thermal expansion coefficient, high mechanical strength, and low electrical conductivity at room temperature. It is used for laser radiation converters [77], as substrates for thermostable surface [78–80] and bulk acoustic wave based devices [81], in piezoelectric non-linear optical devices for second harmonic generation [82–84], in electroacoustic devices [85–87], for pyroelectric sensors [87, 88] and for thermoluminescent dosimetry of x-ray, gamma and neutron radiation [89–91]. LTB was also found to be a Li^+ ion conductor along the (001) direction (polar axis) at high temperatures [92–98].

Considering this technological importance, it is rather surprising that only a limited number of experimental investigations on the electronic structure [99–101] are available in the literature so far. In order to fill the gap, we have performed systematic theoretical investigations of all known Li_2O – B_2O_3 compounds.

3. Computational methods

Bulk and defect properties of Li_2O – B_2O_3 compounds were obtained from periodic calculations with three methods at the DFT level. The Perdew–Wang correlation functional based on the generalized gradient approximation (PW91) [102, 103] was combined with two different exchange functionals. In the PW1PW hybrid method, the exchange functional is a linear combination of the Hartree–Fock expression (20%) and the Perdew–Wang exchange functional (80%) [104]. The second approach is the original PW91 DFT method [102, 103]. For comparison, we also used the well-known B3LYP hybrid method [105, 106] in some cases. These DFT approaches were used as implemented in the crystalline orbital program CRYSTAL [107]. In CRYSTAL the Bloch functions are linear combinations of atomic orbitals (LCAO), expressed as contracted Gaussian functions. The quality of the atomic basis sets determines the reliability of the results. Therefore, we have tested different basis sets in this study. We started with a 6-1G basis [108] for Li. In the second set, a 6-11G Li basis was used where the outer sp exponent was optimized in $\text{Li}(\text{OH})\text{H}_2\text{O}$ [109]. The third Li basis set used is 7-11G* [110]. The 7-11G* basis for Li was further extended to 7-11G(2d) in our previous study [13]. The inner 1s and 2sp shells remained unchanged while the orbital exponents of the 3sp and d shells were optimized for bulk Li_2O at PW1PW level [13]. For boron, a 6-21G* [111] was used, where the outer sp exponent was optimized for BN. The 6-21G* basis set of B was augmented with a second d shell, 6-21G(2d), in our studies [13, 14].

For O, first a 8-411G basis was used as optimized for Li_2O by Dovesi *et al* [21]. The second O basis set was 8-411G* [112]. The 8-411G* basis set was further extended to 8-411G(2d) by adding one more d polarization function. Five combinations of these atomic basis sets (BS) were applied, BS A (Li: 6-1G, B: 6-21G*, O: 8-411G), BS B (Li: 6-11G, B: 6-21G*, O: 8-411G*), BS C (Li: 7-11G*, O: 8-411G*), BS D (Li: 7-11G(2d), B: 6-21G(2d), O: 8-411G*), and BS E (Li: 7-11G(2d), O: 8-411G(2d)). Integration in reciprocal space was performed with a Monkhorst net [120] using shrinking

factors $s = 8$. For the numerical accuracy parameters, we have used stricter values compared to the CRYSTAL defaults.

We also employed the PW91 method implemented in the plane-wave program VASP [113–115]. In this way the effect of complementary types of basis sets, atom-centred functions and delocalized plane waves, on the results obtained with the same density-functional method could be studied. In contrast to the LCAO approach, which allows the explicit treatment of all electrons, inner electrons are replaced by effective potentials in VASP. In our study, the projector augmented wave (PAW) method [116, 117] was used for the core electron representation. Accordingly, the approach was denoted as PW91–PAW. In plane-wave methods the quality of the basis set is determined by a single parameter, the energy cutoff E_{cut} . Three energy cutoff values, $E1 = 400$ eV, $E2 = 520$ eV, and $E3 = 600$ eV, were used. Here $E1$ is the standard value obtained from the VASP guide [118], while $E2$ and $E3$ correspond to increased quality for convergence tests.

4. Bulk properties

In this section we present our results for the structural, energetic and electronic properties for stoichiometric Li_2O [10], B_2O_3 [11], LiBO_2 [12, 13] and $\text{Li}_2\text{B}_4\text{O}_7$ [13, 14].

4.1. Lithium oxide (Li_2O)

Lithium oxide has anti-fluorite structure (space group $Fm\bar{3}m$). The lattice consists of a primitive cubic array of Li^+ ions with spacing $a/2$ where the O^{2-} ions occupy alternating cube centres. The lattice parameter a has been measured at different temperatures in the range 293–1603 K, using coherent inelastic neutron scattering on single crystals and polycrystals [27]. An extrapolation to $T = 0$ K gives $a = 4.573$ Å, about 0.05 Å smaller than the room temperature value, 4.619 Å [119]. The experimental value of the heat of atomization is 1154 kJ mol^{−1} [52] and the fundamental bandgap (E_g) is 7.99 eV [32].

In our theoretical study [10], we have performed a detailed investigation on the structural, energetic and electronic properties for stoichiometric Li_2O . For the CRYSTAL calculations (obtained with the PW1PW, B3LYP, and PW91 methods), the lattice parameter a is converged with the medium quality BS B, the cohesive energy E_{coh} and the optical bandgap E_g are converged with BS D. For the PW91–PAW implementation in VASP, the calculated properties are converged with energy cutoff $E_{\text{cut}} = E2$. Only the converged values are presented in table 1. The lattice parameters obtained with all methods range from 4.56 to 4.64 Å, close to the range of experimental values. All theoretical methods give close agreement with experiment for E_{coh} with deviations of less than $\approx \pm 30$ kJ mol^{−1}.

The band structure was computed along the way that contains the highest number of high-symmetry points of the Brillouin zone (BZ) [121], namely $W \rightarrow L \rightarrow \Gamma \rightarrow X \rightarrow W$. The converged fundamental bandgap (E_g) values are given in table 1. They range from 5.00 eV (PW91–PAW) to 8.11 eV (B3LYP). The converged values of minimum vertical

Table 1. Optimized lattice parameter a (Å), cohesive energy per Li_2O unit E_{coh} (kJ mol^{-1}), and fundamental bandgap E_g (eV); dependence on basis set (BS) and cutoff energy E_{cut} . Only converged values from [10] are shown.

Method	BS, E_{cut}	a	E_{coh}	E_g
PW1PW ^a	D	4.58	−1134	7.95
B3LYP ^a	D	4.59	−1123	8.11
PW91 ^a	D	4.63	−1164	5.82
PW91–PAW ^b	E2	4.64	−1176	5.00
Exp.		4.573 ^c , 4.619 ^d	−1154 ^e	7.99 ^f

^a CRYSTAL results.^b VASP results.^c Reference [27], extrapolated to $T = 0$ K.^d Reference [119], at room temperature.^e Reference [52].^f Reference [32].

transition (MVT) and minimum indirect transition (MIT) energies are given in table 2. For the LCAO based approaches (PW1PW, B3LYP and PW91), the minimum energy gap is indirect in the Γ –X direction. In contrast, with PW91–PAW the Γ – Γ transition is lower than Γ –X (table 2), irrespective of the cutoff energy. In order to check whether this discrepancy is due to the description of core electrons by effective potentials, we performed CRYSTAL PW91 test calculations where the 1s electrons of Li and O were replaced by Stuttgart–Dresden (SDD) effective core potentials (ECP) [122, 123]. As can be seen in table 2, the difference between Γ – Γ and Γ –X is reduced in this way, whereas other transitions except L– Γ are not affected significantly. Therefore, we conclude that the qualitative difference between PW91 (LCAO) and PW91–PAW is caused by the inaccurate representation of core electrons by effective core potentials. The present discussion is only of qualitative nature because of the differences between the SDD-ECP and PAW approaches.

The best agreement for the experimental value of E_g is obtained with the PW1PW method (converged with BS D). Only direct (allowed) transitions are considered since indirect transitions should appear with much lower intensities in optical spectra. The calculated value of E_g is 7.95 eV, close to the experimental value of 7.99 eV [32]. The second best agreement is obtained with the B3LYP method, 8.11 eV (BS D). The two pure Perdew–Wang implementations, LCAO based PW91 and plane wave based PW91–PAW,

underestimate the bandgap. With PW1PW and B3LYP the converged MIT energies (6.94 eV and 7.19 eV, respectively) closely resemble the measured absorption energy at low temperatures, 7.02 eV [29].

A density of states (DOS) calculation with PW1PW shows that the valence band (VB) is mainly formed by the oxygen 2p orbitals with only small contributions from Li, whereas the conduction band (CB) is dominated by Li states. The calculated valence band width is about 5.5 eV which is in good agreement with the experimental value of 5 eV [25]. All other methods give similar results.

4.2. Boron oxide (B_2O_3)

In this section, the geometrical, energetic and electronic properties of both space groups, $P3_121$ (152) and $P3_1$ (144), of B_2O_3 –I are discussed briefly as obtained in our previous study [11]. In particular, the lattice parameters, B–O bond lengths, cohesive energy E_{coh} , and fundamental bandgap E_g are calculated and compared to available experimental data. The relative stability of two B_2O_3 –I structures with space group symmetries $P3_121$ and $P3_1$ was calculated, as both space groups were discussed in the experimental literature [49].

In the $P3_121$ structure the BO_3 triangles are almost planar. All boron atoms are equivalent and only two inequivalent O atoms are present. They are coordinated to two B atoms (figure 2(a)). In the previously suggested less symmetric $P3_1$ structure [50], the B atoms can be separated into types B_1 and B_2 which form two slightly different BO_3 units (figure 2(b)). The three inequivalent O atoms bonded to B_1 (B_2) are labelled as O_1 , O_2 , and O_3 (O'_1 , O'_2 , and O'_3).

The calculated values for the bandgap E_g , the lattice parameters a and c , the B–O bond distances, and the cohesive energies E_{coh} of the optimized structures are compared with experimental values in table 3. For simplicity, here we discuss the results obtained with the PW1PW and PW91–PAW approaches only. For the calculations with the LCAO based approach (PW1PW), basis set B (BS B) is used for B and O as described in the computational method section, whereas PW91–PAW calculations were performed with energy cutoff $E_{\text{cut}} = E2$.

In previous studies [10, 13, 14, 104], it was found that the hybrid method PW1PW gives the closest agreement

Table 2. Minimum vertical transition (MVT) and minimum indirect transition (MIT) energies (eV) of Li_2O bulk obtained with CRYSTAL and VASP. Only converged values from [10] are shown.

Method	BS, E_{cut}	MVT				MIT		
		L–L	W–W	X–X	Γ – Γ	W–L	L– Γ	Γ –X
PW1PW ^a	D	12.05	10.91	8.47	7.95	13.20	8.45	6.95
B3LYP ^a	D	12.24	11.11	8.67	8.11	13.38	8.60	7.19
PW91 ^a	D	9.70	8.71	6.42	5.82	10.73	6.26	5.05
	SDD ^b	9.54	8.78	6.54	5.38	10.60	5.82	5.18
PW91–PAW ^c	E2	9.58	7.69	8.26	5.00	9.59	5.42	7.80

^a CRYSTAL results.^b The inner electrons of Li and O are described by Stuttgart–Dresden ECPs [122, 123].^c VASP results.

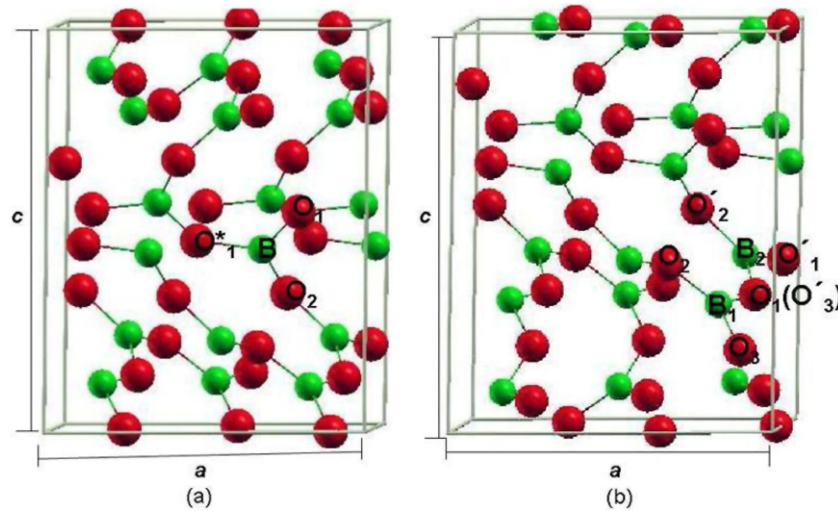


Figure 2. B_2O_3 conventional unit cell for (a) the $P3_121$ space group: B represents boron atom, O_1 and O_2 represent two inequivalent oxygen atoms; and (b) the $P3_1$ space group: B_1 and B_2 represent two inequivalent boron atoms and O_1 , O_2 and O_3 (O'_1 , O'_2 and O'_3) represent three inequivalent oxygen atoms. O: red spheres, B: green spheres.

Table 3. Comparison of calculated B_2O_3 -I lattice parameters a and c (Å), bond distances (Å), cohesive energy E_{coh} (kJ mol⁻¹), and bandgap E_g (eV) with the experimental values as discussed in [11].

Space group $P3_121$			
Properties	PW91-PAW	PW1PW	Exp.
a	4.36	4.35	4.34 ^a
c	8.38	8.39	8.34 ^a
$B-O_1$ ^b	1.384	1.376	1.375 ^a
$B-O_1$	1.381	1.374	1.373 ^a
$B-O_2$	1.376	1.370	1.356 ^a
E_{coh}	-3368.9	-3162.4	-3127 ^c
E_g	6.1	9.1	(6.2) ^d
Space group $P3_1$			
a	4.36	4.37	4.34 ^c
c	8.38	8.40	8.34 ^e
B_1-O_1	1.384	1.383	1.404 ^e
B_1-O_2	1.381	1.380	1.366 ^e
B_1-O_3	1.376	1.375	1.337 ^e
$B_2-O'_1$	1.383	1.385	1.401 ^e
$B_2-O'_2$	1.382	1.382	1.384 ^e
$B_2-O'_3$	1.376	1.378	1.336 ^e
E_{coh}	-3368.6	-3160.7	-3127 ^c
E_g	6.3	8.8	(6.2) ^d

^a Reference [49].

^b Symmetry code other than x, y, z : $-x + 1, -x + y + 1, -z + 1/3$.

^c Reference [52].

^d Previous LDA result [55].

^e Reference [50].

with measured band gaps. This method is therefore taken as reference. With PW1PW, E_g is 9.1 eV ($P3_121$) and 8.8 eV ($P3_1$). Both values are much higher than $E_g = 6.2$ eV as obtained by Li *et al* at the LDA level [55]. This is consistent with the well-known underestimation of band gaps by the LDA [24, 26]. The deficiency is removed with the hybrid

methods, but not with the GGA DFT method. PW91-PAW gives a similar value ($E_g = 6.3$ eV) to the LDA [55].

The best agreement with the experimental lattice parameters is obtained with the hybrid PW1PW approach which overestimates a and c by only 0.01 Å and 0.05 Å respectively. Also the fractional coordinates are close to those proposed in the structure refinement [49]. With all methods, the geometry parameters of the structures with space groups $P3_121$ and $P3_1$ are virtually the same. The bond lengths and lattice parameters agree within 0.01 Å or less. This is not the case for the two proposed structures based on different analyses of the same x-ray spectra [49, 50]. Consequently, the disagreement between theory and experiment is quite large for the second structure with $P3_1$ symmetry [50]. In particular, the B_1-O_3 bond length, which is 1.336–1.337 Å according to the experimental analysis, is overestimated by 0.04 Å with all methods (table 3). Thus, differently from the structure with $P3_121$ symmetry, the low-symmetry structure is not confirmed by the calculations.

PW1PW gives the best agreement with the experimental value for E_{coh} . The deviation is -35 kJ mol⁻¹ (table 3). With both methods, the $P3_121$ structure is slightly more stable than the $P3_1$ structure. The energy difference, about 1 kJ mol⁻¹, is certainly beyond the absolute accuracy of the quantum-chemical methods as shown above. But since two similar structures are compared here, the intrinsic errors of the various approaches are essentially cancelled. All methods predict the $P3_121$ structure as minimum. Moreover, a full optimization of all fractional coordinates without symmetry restrictions at the PW1PW level led to negligible deviations with respect to the symmetric ($P3_121$) structure, and no significant energy lowering was obtained. Thus we conclude that the global minimum structure of B_2O_3 -I has the higher space group symmetry $P3_121$. This confirms the recent reassignment [49].

Table 4. Comparison of calculated and experimental lattice vectors a , b , c (Å) and β (deg), cohesive energy E_{coh} per LiBO_2 unit (kJ mol^{-1}) and bandgap E_g (eV) [12].

Lattice parameter	PW1PW	PW91-PAW	Exp. ^{a,b}
a	5.82	5.84	5.85
b	4.37	4.39	4.35
c	6.48	6.60	6.45
β	114.89	114.38	115.09
E_{coh}	-2230	-2340	-2238
E_g	8.19	5.74	

^a Experimental reference for structural data [124].^b Experimental reference for cohesive energy [125].**Table 5.** Comparison of calculated and experimental lattice vectors a and c (Å), cohesive energies E_{coh} per $\text{Li}_2\text{B}_4\text{O}_7$ unit (kJ mol^{-1}) and bandgap E_g (eV) [14].

Lattice parameter	PW1PW ^a	PW91-PAW ^b	Exp. ^{c,d}
a	9.50	9.57	9.48
c	10.32	10.39	10.29
E_{coh}	-7683	-8127	-7658
E_g	9.31	6.22	

^a Obtained with CRYSTAL.^b Obtained with VASP.^c Reference for experimental lattice parameters [128].^d Reference for experimental cohesive energy [125].

4.3. Li_2O - B_2O_3 mixed compounds

As stated before, the binary Li_2O - B_2O_3 system is characterized by the formation of nine lithium borate compounds, namely Li_3BO_3 , α - $\text{Li}_4\text{B}_2\text{O}_5$, β - $\text{Li}_4\text{B}_2\text{O}_5$, $\text{Li}_6\text{B}_4\text{O}_9$, LiBO_2 , $\text{Li}_2\text{B}_4\text{O}_7$, $\text{Li}_3\text{B}_7\text{O}_{12}$, LiB_3O_5 , and $\text{Li}_2\text{B}_8\text{O}_{13}$ [57–60]. Of them LiBO_2 [72, 73] and $\text{Li}_2\text{B}_4\text{O}_7$ [92–98] were found to be Li^+ ion conductors. Therefore we have studied the structural, energetic and electronic properties of stoichiometric and defective LiBO_2 [12, 13] and $\text{Li}_2\text{B}_4\text{O}_7$ [13, 14, 17]. Here we present the bulk properties of these two systems. Calculations with LCAO based approaches were performed with basis set B (BS B), whereas plane wave based calculations were performed with energy cutoff $E_{\text{cut}} = E2$.

4.3.1. Lithium metaborate (LiBO_2). LiBO_2 belongs to space group $Pn2_1/c$ of monoclinic class with measured lattice parameters $a = 5.85$ Å, $b = 4.35$ Å, $c = 6.45$ Å, and $\beta = 115^\circ$ [124]. The experimental value of heat of formation or atomization of crystalline LiBO_2 is -2238 kJ mol^{-1} [125]. In our theoretical study [12], we have performed a detailed investigation on the structural, energetic and electronic properties of LiBO_2 . Here we discuss the optimized lattice parameters, cohesive energy E_{coh} per LiBO_2 formula unit and fundamental bandgap E_g , as obtained with the PW1PW method using CRYSTAL and with PW91-PAW using VASP (table 4).

The PW1PW method gives the best agreement for the lattice parameters with experimental values (table 4), namely the deviation is less than ± 0.03 Å for a , b and c and 0.40° for β .

As for Li_2O and B_2O_3 , the PW1PW method gives the best reproduction of the experimental cohesive energy for LiBO_2 . With this method E_{coh} is only 8 kJ mol^{-1} smaller than the experimental value. With PW91-PAW, the difference is larger, namely -102 kJ mol^{-1} . This is in line with the previous investigation with LTB [14]. One possible reason for these differences between the LCAO and plane wave based cohesive energies is that the atomic reference energies obtained with plane waves are too high.

The electronic structure, namely the band structure and DOS of crystalline LiBO_2 , were calculated with different methods [12, 13]. The band structure was calculated along the path that contains the highest number of high-symmetry

points of the Brillouin zone [121] ($Z \rightarrow C \rightarrow Y \rightarrow \Gamma \rightarrow B \rightarrow D \rightarrow C$). All considered methods indicate that the LiBO_2 crystal has an indirect (Γ -B) bandgap (E_g). However, the direct Γ - Γ transition energy is only slightly larger. The difference does not exceed 0.08 eV.

According to our results, LiBO_2 is a wide-gap insulator. The VBs are characterized by a lack of dispersion and there are minigaps all over the VB region. This type of band structure signifies that the electronic states are more or less dictated by the localized B-O bonding units. As a result, the hole effective masses are very large, which is typical of wide-gap insulators [126]. With all the considered DFT methods, the top of the VB is at the point Γ , and the bottom of the CB is at B . The values of E_g vary from 5.74 eV (PW91-PAW) to 8.19 eV (PW1PW) due to different amounts of self-interaction error.

The density of states (DOS) was calculated using the Fourier-Legendre technique [127] with a Monkhorst net [120] using the shrinking factor $s = 8$. The valence band is composed of O 2p states and B-O bonding states of BO_3 triangles. Its width is about 10 eV. Li has almost no contribution in the VB. The bottom of the CB is dominated by the contribution from B atoms and comparatively less by the contribution from Li.

4.3.2. Lithium tetraborate ($\text{Li}_2\text{B}_4\text{O}_7$). The LTB lattice belongs to space group $I4_1cd$ and has 104 atoms per unit cell [128] with measured lattice parameters $a = 9.48$ Å and $c = 10.29$ Å. The main structural pattern is a $[\text{B}_4\text{O}_9]^{6-}$ (as shown in figure 3) complex which consists of two planar trigonal (BO_3) and two tetrahedral (BO_4) units. The lithium atoms are located at interstices [128], as shown in figure 3.

In our theoretical study [14], we have performed detailed investigation on structural optimization such as calculations of lattice parameters, bond distances and angles, and energetics and electronic properties with PW1PW, PW91 and B3LYP using CRYSTAL, and with PW91-PAW using VASP. Here we present only the basis set converged values obtained with PW1PW and PW91-PAW, in table 5, together with the corresponding experimental values.

The PW1PW method gives the best reproduction of the experimental values for a and c ($\Delta a = +0.02$ Å, $\Delta c = +0.03$ Å) (table 5).

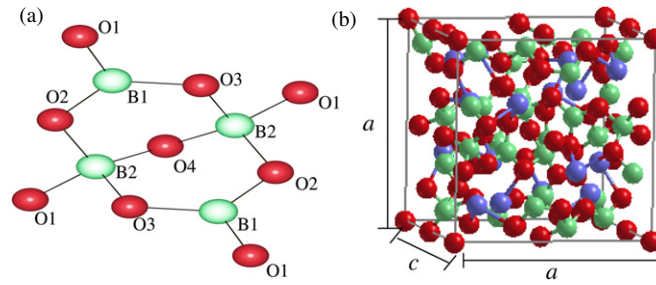


Figure 3. The main structure elements (anion $[B_4O_9]^{4-}$) consisting of $B_{(1)}O_3$ and $B_{(2)}O_4$ units and the unit cell of $Li_2B_4O_7$ crystal; Li: blue spheres, O: red spheres, B: green spheres.

Table 6. The values of vertical electronic transitions and minimum transition (MT) energies (eV) for $Li_2B_4O_7$ calculated with different methods [14].

Transition		PW1PW	PW91-PAW
Γ	Γ	9.41	6.27
N	N	9.55	7.08
P	P	9.75	7.31
X	X	9.72	7.22
M	M	9.42	6.96
MT	M- Γ	M- Γ	M- Γ
Value		9.31	6.22

The calculated cohesive energies E_{coh} per $Li_2B_4O_7$ formula unit are compared with the experimental value [125] in table 5. The best agreement with the experimental E_{coh} is obtained with the PW1PW approach with a deviation of 25 kJ mol^{-1} . With PW91-PAW (VASP) the difference is very large, -279 kJ mol^{-1} .

Only a small number of theoretical and experimental investigations of electronic spectra for crystalline $Li_2B_4O_7$ were found in the literature [99–101]. The electronic structure, namely the valence band, of LTB has been experimentally studied by x-ray photoelectron spectroscopy (XPS) [100] in combination with a theoretical investigation based on local density approximation (LDA) calculations of the free anion $[B_4O_9]^{6-}$.

In our studies [13, 14], the band structure was calculated along the path that contains the highest number of high-symmetry points of the Brillouin zone [121] ($M \rightarrow \Gamma \rightarrow X \rightarrow P \rightarrow N$). With all the considered methods, the top of the VB is at the point M, and the bottom of the CB is at Γ . Converged values of vertical VB–CB transitions in $Li_2B_4O_7$ and minimum transition energies are presented in table 6.

All the considered methods indicate that the LTB crystal has an indirect (M- Γ) bandgap E_g . However, the direct Γ – Γ transition energy is only slightly larger. The difference does not exceed 0.10 eV. The values of E_g vary from 6.22 eV (PW91-PAW) to 9.31 eV (PW1PW).

The analysis of DOS shows that LTB has very sharp VB and CB edges. The states near the VB top are mainly created by oxygen 2p states. The contributions from atomic orbitals of other atoms (Li, B_1 —boron in BO_3 , and B_2 —boron in BO_4) are ten times smaller than the oxygen PDOS. The bottom of the CB is dominated by contributions from B_1 atoms. It should

be noted that orbitals from Li and B_2 atoms are not involved in low-energy band–band transitions since their contributions to the lower part of the CB are very small.

5. Surface properties

Recent studies [1–3] show that the Li ion conductivity in $Li_2O:B_2O_3$ nanocomposites is higher than in Li_2O , although B_2O_3 is an insulator. This is due to an increased fraction of structurally disordered interfacial regions and an enhanced surface area [1]. It is assumed that the interfacial region between Li_2O and B_2O_3 nanocrystals is formed by the combination of stable surfaces of the corresponding bulk materials. The most stable Li_2O surfaces are (111) and (110) [15, 130, 131]. For the first time, we have studied several low-index surfaces of B_2O_3 [16] such as (101), ($\bar{1}\bar{1}\bar{1}$), (100) and (001).

Here we review the studies on structure, stability and electronic properties of low-index surfaces of Li_2O and B_2O_3 . The calculations were performed by the PW1PW method with BS A and BS B for Li_2O surfaces and BS B for B_2O_3 surfaces. The relative stability of the surfaces was estimated according to their surface energy (E_s), calculated as

$$E_s = \frac{E_{slab} - mE_{bulk}}{2A} \quad (1)$$

where E_{slab} is the total energy of the two-dimensional slab with m Li_2O or B_2O_3 formula units, E_{bulk} is the total energy per unit of the Li_2O or B_2O_3 bulk, again taken from our previous study [10, 11], and A is the surface area of the slab. The division by 2 in equation (1) implies that the slab has two identical surfaces. Our slab models were constructed according to this requirement. They either contain a central mirror plane, an inversion centre, or a two-fold axis. In this way artificial polarization effects due to dipole moments along the surface normal are avoided.

5.1. Surfaces of Li_2O

The (111) and (110) surfaces were modelled with a series of slabs with increasing number of atomic layers ($n = 3, 6, 9, 12, 15, 18, 21, 24$ and $n = 2, 4, 5, 6, 10$, respectively) [15]. Here we discuss the results obtained with basis set BS B only. The lattice parameters of the slab were obtained from the optimized PW1PW bulk values of our previous investigation

Table 7. Convergence of calculated surface energies E_s (J m^{-2}) of $\text{Li}_2\text{O}(111)$ and $\text{Li}_2\text{O}(110)$ with the number n of atomic layers in the slab model (method: PW1PW, basis set (BS): B) [15].

$\text{Li}_2\text{O}(111)$			$\text{Li}_2\text{O}(110)$		
n	E_s (unrelaxed)	E_s (relaxed)	n	E_s (unrelaxed)	E_s (relaxed)
3	0.815	0.799	2	1.363	1.118
6	0.819	0.789	4	1.433	1.224
9	0.820	0.790	5	1.438	1.243
12	0.821	0.790	6	1.438	1.240
15	0.822	0.794	10	1.440	1.240
18	0.823	0.793	15	1.442	1.247
21	0.825	0.795			
24	0.823	0.793			

on Li_2O [10] using the same basis sets. All atomic layers of the slab models were fully relaxed.

The relative stability of the surfaces was estimated according to their surface energy (E_s), calculated with equation (1). As the models are finite in the direction of the surface normal, convergence with the number n of layers has to be checked. In table 7, the surface energies and their convergence with increasing number of layers (n) are presented for unrelaxed and relaxed slabs. For both surfaces, fast convergence with n was obtained, in line with the ionic character of lithium oxide.

E_s has converged within 0.001 J m^{-2} with a six-layer slab for $\text{Li}_2\text{O}(111)$ (table 7), and with a five-layer slab for $\text{Li}_2\text{O}(110)$ (table 7). There is a slightly larger relaxation effect for the (110) surface compared to the (111) surface. The converged E_s value of the (111) surface is 0.79 J m^{-2} , significantly smaller than that of the (110) surface, 1.24 J m^{-2} . The relative stability of the two surfaces agrees well with the *ab initio* study of Li_2O surfaces by Lichanot *et al* [131].

Li_2O is a wide-gap (bandgap 7.99 eV) insulator [32]. The calculated bandgap obtained with the PW1PW method (BS D) is 7.95 eV [10], which agrees reasonably well with experiment. The qualitative features of the projected DOSs of both the surfaces are similar to those of the bulk [15]: the valence band (VB) is mainly formed by the oxygen 2p orbitals with only small contributions from Li, whereas the conduction band (CB) is dominated by Li states. However, there is an upward shift of the VB top and a downward shift of the CB bottom for the surfaces, thereby reducing the bandgap compared to the bulk. This is in agreement with an electronic-energy-loss spectroscopic (EELS) study on the surface valence-to-conduction band transition for Li_2O [25]. According to our results, surface excitons are more pronounced in the case of the Li_2O (110) surface [15].

5.2. Surfaces of B_2O_3

Our study [16] was focused on the low-index B_2O_3 surfaces $(101) \equiv (011)$, $(\bar{1}\bar{1}1)$, $(100) \equiv \{(010), (\bar{1}10)\}$ and (001) . High-index surfaces cannot be completely ruled out, but they are usually not the most stable oxide surfaces and are often found to reconstruct by forming facets of low-index surfaces [132].

The relative stability of the surfaces was estimated according to their surface energy (E_s), calculated with

Table 8. Convergence of surface energies E_s (J m^{-2}) with number of layers n for B_2O_3 -I surfaces (101), $(\bar{1}\bar{1}1)$, (100), and (001) (method: PW1PW, basis set (BS): B) [16].

Surface n	(101)	$(\bar{1}\bar{1}1)$	(100)	(001)
15	0.56	1.09	1.56	2.18
30	0.30	1.11	1.28	2.18
45	0.34	1.12	1.29	2.21

equation (1). The lattice parameters of the slab were obtained from the optimized PW1PW values of the bulk [11]. All atomic layers of the slab models were fully optimized. The primitive bulk unit cell (PBU) contains 15 atoms (B_6O_9). Here the selected (101), $(\bar{1}\bar{1}1)$, (100) and (001) surfaces are all oxygen-terminated and have either a central C_2 axis or a screw axis perpendicular to the surface normal.

In accordance with the above considerations we used $n = 15, 30$ and 45 . Only for the $(\bar{1}\bar{1}1)$ surface we also considered 60 layers. In table 8, the convergence of E_s with slab thickness is presented for optimized slabs.

The most stable surface is (101). For this surface, a rather slow convergence of the surface energy with the number of layers was observed. E_s is converged within 0.04 J m^{-2} only with the 45-layer slab. During optimization, the surface is reshaped. New B–O bonds, not existing in the bulk, are formed in the top-most layers.

The situation is quite different for the second most stable $(\bar{1}\bar{1}1)$ surface. This is due to much larger atomic displacements (up to 1.8 \AA) extending into the centre of the slab. Even in the inner-most layers of the largest 60-layer slab atoms are moved by more than 0.4 \AA . Therefore, no convergence of structural properties with n was obtained.

For the (100) surface, the convergence with respect to the number of layers is slow. There are as well changes of the atomic coordination at the surface during optimization. The nearest-neighbour B–B bond distance decreases from 2.51 to 2.39 \AA during optimization. In spite of the similar stabilization energy compared to the $(\bar{1}\bar{1}1)$ surface, the atomic displacement steadily decreases with increasing distance from the surface. We conclude that the 45-layer model is large enough to represent the (100) surface.

The smallest change of atomic coordination upon optimization is observed for the (001) surface. In general, the displacements are smaller than those for the other surfaces

(<0.6 Å). The convergence of the surface energy with respect to the number of layers is comparably fast. E_s (2.21 J m⁻²) is converged within 0.03 J m⁻² already with the smallest 15-layer slab.

The relative stability of the four investigated surfaces can be qualitatively understood by the number of broken B–O bonds per surface unit. The numbers of broken bonds per surface unit cell are initially 2, 4, 4 and 2 for the (101), (111), (100) and (001) surfaces, respectively. After optimization, the numbers of ‘dangling bonds’ are reduced to 0, 2, 2 and 1, respectively. These correspond to 0.0, 0.05, 0.05, and 0.06 bonds Å⁻². The trend is qualitatively in line with the order of the calculated surface energies, 0.34, 1.12, 1.29 and 2.21 eV (table 8).

The qualitative features of the PDOSs of the (101) surface and the bulk are rather similar [16]. In both systems the valence band (VB) is mainly composed of oxygen 2p orbitals and the lower part of the conduction band (CB) mainly consists of boron orbitals. The VB width is almost the same, ≈9 eV. However, the bandgap of the (101) surface is only 8.5 eV. A closer look reveals the presence of occupied surface states between 0 and -0.2 eV, separated by a small gap of 0.1 eV from the VB. The largest contributions of these states are from first- and second-layer oxygens. Although there are no dangling bonds in the optimized surface, the different Madelung potential experienced by the top-most atoms leads to a shift of the corresponding levels to higher energies. The PDOSs of the less stable (111) and (100) surfaces show features similar to those of the (101) surface. The defect states are even more pronounced in these cases.

6. Defects and diffusion in Li₂O

In this section, we review our studies on defects and ionic conduction in Li₂O bulk [10] and surfaces [15].

The formation energy of a cation vacancy $E_{\text{de}}(\text{V})$ is calculated with the following equation:

$$E_{\text{de}}(\text{V}) = E^{\text{SCM}}(\text{V}) + E(\text{Li}) - E^{\text{SCM}}. \quad (2)$$

Here $E^{\text{SCM}}(\text{V})$ and E^{SCM} denote the total energy of the supercell model with and without a vacancy, respectively, and $E(\text{Li})$ is the energy of the free Li atom in its ground state.

The formation energy of an anion vacancy $E_{\text{de}}(\text{F})$ is calculated with the following equation:

$$E_{\text{de}}(\text{F}) = E^{\text{SCM}}(\text{V}) + E(\text{O}) - E^{\text{SCM}}. \quad (3)$$

Here $E^{\text{SCM}}(\text{V})$ and E^{SCM} denote the total energy of the supercell model with and without a vacancy, respectively, and $E(\text{O})$ is the energy of the free O atom in its ground state.

To create a cation vacancy, one Li atom was removed from the supercell keeping the system neutral. Thus the supercell contained an odd number of electrons and its ground state was a doublet. The calculations were performed with the spin polarized method (unrestricted Kohn–Sham, UKS). To create an F centre, one neutral oxygen atom was removed from the supercell. Calculations were performed for the closed shell singlet state.

Table 9. Converged cation vacancy $E_{\text{de}}(\text{V})$ and F centre $E_{\text{de}}(\text{F})$ formation energies (kJ mol⁻¹) for the Li₆₄O₃₂ supercell.

Method	PW1PW	PW91–PAW
BS, E_{cut}	B	E2
$E_{\text{de}}(\text{V})$ (unrelaxed)	642	558
$E_{\text{de}}(\text{V})$ (relaxed)	576	480
$E_{\text{de}}(\text{F})$ (unrelaxed)	878	975
$E_{\text{de}}(\text{F})$ (relaxed)	873	957

The Frenkel formation energy $E_{\text{de}}(\text{Fr})$ is the energy needed to move a Li⁺ ion from its regular lattice site to an interstitial site.

6.1. Li₂O bulk

In the present study, cation vacancy and F centre defects in bulk Li₂O are discussed as investigated in our theoretical study [10]. In order to minimize direct defect–defect interaction between neighbouring cells, we used a large supercell (Li₆₄O₃₂) as a model of the defective bulk. It was obtained from the primitive unit cell by a transformation with matrix **L**:

$$\mathbf{L} = \begin{pmatrix} -2 & 2 & 2 \\ 2 & -2 & 2 \\ 2 & 2 & -2 \end{pmatrix}. \quad (4)$$

In order to study the convergence behaviour of the calculated defect properties we also considered the smaller supercell Li₃₂O₁₆. The formation energies of the cation vacancy and F centre are calculated with equations (2) and (3) respectively for unrelaxed and fully relaxed systems. In table 9, we present only the converged values of $E_{\text{de}}(\text{V})$ and $E_{\text{de}}(\text{F})$ obtained with PW1PW using BS B and PW91–PAW using $E_{\text{cut}} = E2$.

6.1.1. Cation vacancy. The converged $E_{\text{de}}(\text{V})$ values with the LCAO based PW1PW approach and the plane wave based DFT method PW91–PAW are 576 kJ mol⁻¹ and 480 kJ mol⁻¹, respectively. The inclusion of exact exchange leads to an increase of the defect formation energy.

The structural relaxation effects are investigated by measuring the changes of the distances of the relaxed atoms from the Li defect position. Here we discuss the results obtained with the PW1PW approach only. All other methods give the same trend. The four O atoms in the first coordination shell (first nearest neighbours, 1-NN) show an outward relaxation from the vacancy, namely by 6.6% with the PW1PW method. This is reasonable, since the electrostatic attraction by the Li⁺ cation is missing. The removal of one neutral Li atom creates a hole in the valence band. One of the surrounding four O atoms (formally O²⁻) in 1-NN becomes O⁻ and the spin density is localized on this O atom. Six Li atoms in the second coordination shell (2-NN) show a strong inward relaxation of -10.0% with the PW1PW approach. Due to the reduced electrostatic repulsion, the 2-NN Li atoms tend to move toward the vacancy. The 12 Li atoms in the third coordination shell (3-NN) show an outward relaxation. All

other atoms with larger distances to the defect position show only small relaxation. Thus the relaxation is mainly restricted to the nearest- and the second-nearest-neighbour atoms.

The DOSs for a defective $\text{Li}_{63}\text{O}_{32}$ supercell were calculated with all the methods. All the methods show qualitatively the same behaviour. The neutral Li vacancy introduces an extra unoccupied level in the β ladder roughly 0.33 eV above the Fermi level (E_F) with the PW1PW approach. The unoccupied defect level consists of oxygen states. The PW1-PAW approach gives nearly the same energetic position of the unoccupied defect level above E_F (0.31 eV).

6.1.2. F centre. For the calculation of the F centre using the LCAO based approaches, the basis functions of the oxygen ion were left at the defect position. Calculations were performed for the closed shell singlet state. A test calculation with the PW1PW method for the triplet state showed that $E_{\text{de}}(\text{F})$ is much higher (by 539 kJ mol^{-1}) for the triplet state than for the closed shell singlet state. The converged value of $E_{\text{de}}(\text{F})$ with PW1PW using BS B is 873 kJ mol^{-1} (table 9). The relaxation energy is very small, $\approx 5 \text{ kJ mol}^{-1}$.

For the plane wave based DFT method, PW91-PAW, the converged value of $E_{\text{de}}(\text{F})$ is 948 kJ mol^{-1} . Compared to the PW1PW method, this value is overestimated by 100 kJ mol^{-1} . The differences between hybrid and pure DFT methods demonstrate the importance of exact exchange in the calculation of defect energies.

The structural relaxation effects of the F centres are investigated by measuring the changes of distances of the relaxed atoms from the defect position. Only the PW1PW results are discussed in the following. All the other methods give qualitatively the same trend. The F centre is surrounded by eight Li atoms in the first coordination shell (1-NN). The Li atoms in 1-NN show an outward relaxation from the vacancy, namely by 1.5% with PW1PW. This is reasonable, since the 1-NN Li atoms are positively charged and should, therefore, repel each other as the central oxygen ion is removed. But the effect is much smaller than for the oxygens surrounding the Li defect. The 12 2-NN O atoms show an outward relaxation of 0.2%, indicating that the positions of the oxygen atoms are almost unchanged. These results agree well with the outward relaxation of 1-NN Li atoms and 2-NN O atoms for the F centres in Li_2O obtained by Tanigawa *et al* [37]. In that study the displacements were even smaller, namely by 0.05% for 1-NN Li atoms and 0.01% for 2-NN O atoms. Further relaxation shows that 24 3-NN Li atoms, six 4-NN O atoms, 24 5-NN Li atoms and 24 6-NN O atoms are unchanged.

The experimental value of the optical transition energy for oxygen deficient Li_2O is 3.7 eV [29], indicating a location of a doubly occupied defect level about 4.3 eV above the valence-band-maximum (VBM). This is reflected by the calculated density of states (DOS) of the defective supercells. With the PW1PW approach, the doubly occupied defect level is located 3.9 eV below the CB edge.

The obtained transition energy is in good agreement with the experimental value of 3.7 eV [29], whereas the PW91-PAW approach gives too small a value of the optical

absorption energy, namely 2.7 eV. This can be related to the artificial self-interaction in DFT methods which is not completely removed in the GGA.

6.1.3. Migration of Li^+ ions. In our previous theoretical study [10], the investigation of Li migration from a regular lattice site to an adjacent vacancy was performed with the PW1PW and B3LYP methods using the CRYSTAL code and the PW91-PAW method using the VASP code. In this section we discuss our results obtained with the PW1PW and PW91-PAW approaches.

In figure 4, the migration process is illustrated. Figure 4(a) shows the unrelaxed structure of defective Li_2O where the migrating Li^+ ion and the vacancy (V) are in their original positions. Figure 4(b) shows the symmetric transition structure. The lithium ion is centred between two oxygen ions. The activation energy E_A for the migration process is calculated from the energy difference between the transition structure (figure 4(b)) and the initial structure (figure 4(a)). The final structure (figure 4(c)), where the migrating ion has accessed the position of the vacancy, is isoenergetic with the starting structure.

The experimental hopping distance for the migration of the Li^+ ion from its original tetrahedral site to the vacancy is the nearest Li-Li distance in Li_2O [27], namely, 2.29 Å. The calculated hopping distances slightly differ for the considered methods due to the different optimized lattice constants. They are 2.28 and 2.29 Å for PW1PW and PW91-PAW respectively. For the calculation of the potential energy curve, the migration path of the Li^+ ion was divided into ten equidistant steps. Our theoretical model corresponds to a single Li ion hop. This process is comparable to that studied with NMR relaxation [1]. Therefore, the calculated activation energies E_A are compared with this experimental value, 0.31 eV [1].

We performed the study of Li^+ migration in three steps. First the potential curve for the movement of Li from its regular position to the nearest defect position was calculated without relaxation of the neighbouring atoms. In the second step the nearest neighbouring atoms around the defect and the migrating Li were relaxed. The vacancy and the migrating ion are surrounded by four oxygens each in the first coordination shell. Together they have six oxygen atoms as nearest neighbours (1-NN). Two oxygens are bridging the two tetrahedra (figure 4(a)). In the defective structure, one unpaired electron is localized on one of these bridging oxygens, mainly in the 2p orbitals. This situation was also observed in previous DFT-LDA investigations for Li^+ ion diffusion in Li_2O [35]. It can be expected that this oxygen atom undergoes pronounced changes in its coordination geometry and that it is important to include it in the relaxation. In the final step, all atoms of the cell were allowed to relax except the migrating Li atom, which was fixed at each predefined position on the migration path.

It can be seen from table 10 (column 2) that both methods significantly overestimate the experimental E_A , if relaxation is not taken into account. The values range from 0.45 eV (PW1PW) to 0.49 eV (PW91-PAW). The barrier is drastically

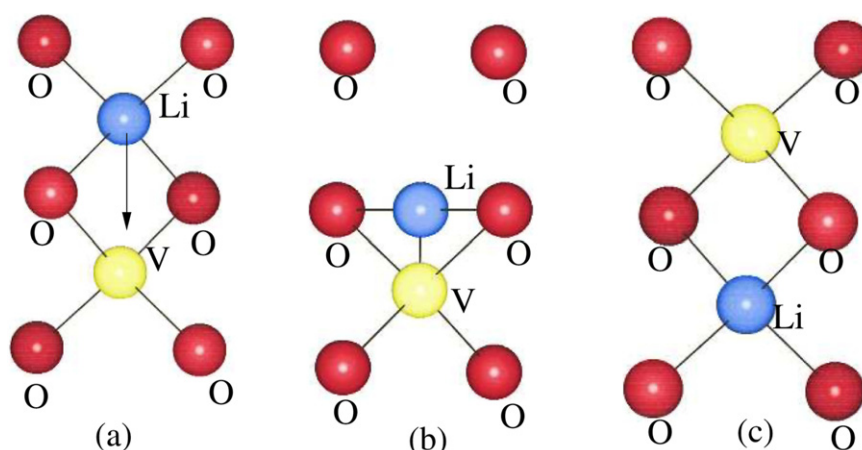


Figure 4. The Li^+ ion migration process in Li_2O . In (a) the Li^+ ion and vacancy (V) are in their original positions, in (b) the transition state and in (c) the migrating Li^+ ion is in the vacancy position while the vacancy is in the original position of the Li^+ ion.

Table 10. Comparison of calculated activation energies for Li migration, E_A (eV), in Li_2O bulk for unrelaxed systems, relaxation of nearest neighbours (1-NN) and fully relaxed systems with experimental values [10].

Method	E_A		
	Unrelaxed	1-NN	Full relaxation
PW1PW	0.45	0.17	0.33 (0.39 ^a)
PW91-PAW	0.49	0.17	0.28 (0.27 ^a)
Exp. ^b			0.31
LDA			0.34 ^c , 0.30 ^d

^a Obtained with a smaller $\text{Li}_{32}\text{O}_{16}$ supercell.

^b Reference [1].

^c Reference [35].

^d Reference [43].

reduced when relaxation of the first neighbours (1-NN) is performed (table 10, column 3).

Surprisingly, the calculated barriers at this level of relaxation (0.17 eV) are even smaller than those with full relaxation of all atoms in the cell (table 10, column 4). One reason for the small barriers obtained with 1-NN relaxation is that the movement of the oxygen atoms surrounding the vacant Li lattice site in figures 4(a) and 4(c) is hindered by the repulsive interaction with their nearest oxygen neighbours which are fixed. The stabilization of the defect structure was 2–3 times larger for the relaxation of the second nearest neighbours compared to the 1-NN relaxation. Apparently, this effect is less pronounced for the transition state structure. A good agreement with experiment was achieved only with full relaxation. The calculated barriers range from 0.28 to 0.33 eV (table 10, column 4). In order to study the dependence of E_A on the supercell size, we also studied the smaller cell $\text{Li}_{32}\text{O}_{16}$ (see values in parentheses in table 10). The PW1PW hybrid method gives a slightly larger barrier (0.39 eV) than the $\text{Li}_{64}\text{O}_{32}$ supercell, whereas for PW91-PAW there is essentially no change (0.27 eV). Similar activation energies (0.34 eV and 0.30 eV) were obtained in plane-wave DFT studies of the $\text{Li}_{32}\text{O}_{16}$ supercell based on the local density

approximation using norm-conserving pseudopotentials [35] and ultra-soft pseudopotentials [43], respectively.

The possibility of a different migration path where the Li^+ ion moves in a two-dimensional curve rotation rather than in a straight line was also investigated. Here only the PW91-PAW method was employed. The energy hypersurface was scanned point-by-point. The lowest energy was found at a location almost identical to the central symmetric position of the straight line. Also the energy barrier E_A for the curve rotation (0.28 eV) was virtually identical to the value of 0.28 eV obtained for the migration in a straight line. Therefore, it can be concluded that the migration of the Li^+ ion occurs in an almost straight line.

6.2. Li_2O surfaces

Two dominant point defect types, cation vacancies and cation Frenkel defects, are studied for the most stable $\text{Li}_2\text{O}(111)$ surface [15]. The convergence of the defect formation energy was checked with respect to increasing supercell size (decreasing defect concentration), increasing number of slab layers and basis set size with the PW1PW approach.

6.2.1. Cation vacancy. Using optimized structural parameters for the perfect crystal [10], 2×2 and 4×4 surface supercells were constructed containing six-, nine- and twelve-layer slabs parallel to the (111) surface for Li_2O . The vacancy was created by removing one Li atom (site A, see figure 5) from the supercell keeping the system neutral.

The formation energy of the cation vacancy $E_{\text{de}}(\text{V})$ was calculated with equation (2) for unrelaxed and fully relaxed systems.

As found for bulk Li_2O [10], $E_{\text{de}}(\text{V})$ has a small BS dependence, the difference between BS A and BS B being only 1–2 kJ mol^{-1} . Therefore, the cation vacancy formation energies obtained only with BS A are presented in table 11. $E_{\text{de}}(\text{V})$ decreases with decreasing defect concentration (i.e. increasing supercell size). This indicates a long-range repulsive interaction between lithium vacancies

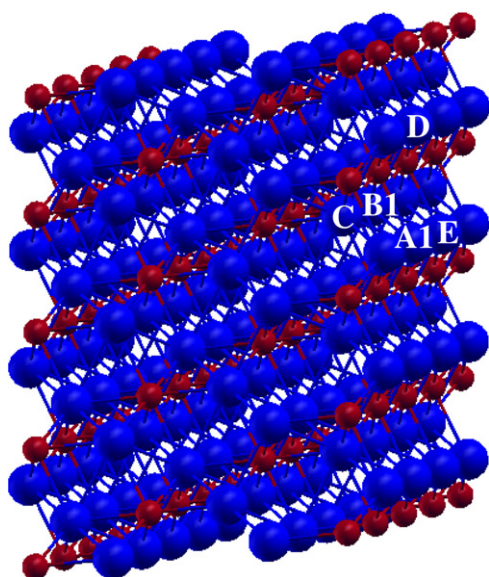


Figure 5. A six-layer slab for the 4×4 supercell of the Li_2O (111) surface. Blue circles represent lithium atoms and red circles represent oxygen atoms.

Table 11. The effect of relaxation on the cation vacancy formation energy $E_{\text{de}}(\text{V})$ (kJ mol^{-1}) in Li_2O (111) (PW1PW method with basis set (BS) A) [15].

Supercell	n	Structure	$E_{\text{de}}(\text{V})$
2×2	6	Unrelaxed	633
		Relaxed	553
	9	Unrelaxed	638
		Relaxed	552
	12	Unrelaxed	641
		Relaxed	552
4×4	6	Unrelaxed	663
		Relaxed	543
	9	Unrelaxed	685
		Relaxed	542
	12	Unrelaxed	710
		Relaxed	543

located in neighbouring cells. The observed trend can also be due to the effect of relaxation of the lattice atoms around the vacancy. The movement of the atoms out of their lattice positions due to the presence of the defect is restricted by the periodic boundary conditions introduced on the supercell. This can be best seen by the smaller relaxation energy of the 2×2 supercell (E_{R} is $\approx 60\text{--}65 \text{ kJ mol}^{-1}$) compared to that of the 4×4 supercell (E_{R} is in the range of $110\text{--}130 \text{ kJ mol}^{-1}$).

For both 2×2 and 4×4 supercells, $E_{\text{de}}(\text{V})$ is converged with six-layer slabs. The converged $E_{\text{de}}(\text{V})$ value for the Li_2O (111) surface is 542 kJ mol^{-1} . This can be compared to the bulk value for Li_2O , 576 kJ mol^{-1} , obtained with the same method and basis sets [10]. Therefore, we conclude that the surface of Li_2O contains a higher percentage of defects than bulk Li_2O .

The calculated geometrical relaxation effects around a Li vacancy are investigated. The three oxygen atoms in the first coordination shell (first nearest neighbours, 1-NN) increase their distance to the vacant Li site by 5%. This is

Table 12. The effect of relaxation on the Frenkel formation energy E_{Fr} (kJ mol^{-1}) for Li_2O (111); 4×4 supercell model; PW1PW method, basis set (BS) A [15].

n	BS A	Exp. (Li_2O [34])	Calc. (Li_2O [10])
6	154	244	216
9	152		

reasonable, since the electrostatic attraction by the Li^+ cation is missing. The removal of one neutral Li atom creates a hole in the valence band. According to a Mulliken population analysis of the crystal orbitals, one of the surrounding 1-NN O atoms (formally O^{2-}) is oxidized to O^- and the spin density is localized on this O atom. Three Li atoms in the second coordination shell (2-NN) show an inward relaxation of -6% . Due to the reduced electrostatic repulsion, the 2-NN Li atoms tend to move toward the vacancy. The nine Li atoms in the third coordination shell (3-NN) show an outward relaxation. All other atoms with larger distances to the defect position show only small displacements. Thus the lattice relaxation is mainly restricted to the nearest- and second-nearest-neighbour atoms of the defect site. This is in line with the structural relaxations around a cation vacancy observed in bulk Li_2O [10].

6.2.2. Cation Frenkel defect. Based on our experience from the cation vacancy investigation, only 4×4 supercells containing six- and nine-layer slabs were employed. To simulate the cation Frenkel defects, one Li atom was removed from the regular site and was placed at interstitial sites at different distances. The lowest Frenkel formation energy (E_{Fr}) was obtained for a distance of 3.60 \AA between the interstitial and the regular sites.

As in the case of cation defects, a small dependence on the model parameters was observed for the Frenkel defect formation: E_{Fr} changes by only $2\text{--}3 \text{ kJ mol}^{-1}$ when the BS is increased from A to B, and by only 1 kJ mol^{-1} when the number of atomic layers is increased from six to nine [15]. Therefore, calculated E_{Fr} values with BS A are presented in table 12.

The similarity of the trends obtained for $E_{\text{de}}(\text{V})$ and E_{Fr} is not surprising since both defects involve the formation of an empty Li lattice site. Due to the different references, the absolute values of E_{Fr} are much smaller than those of $E_{\text{de}}(\text{V})$. The two defect types can be regarded as extreme cases of real lattice defects, where the dislocated Li is close to the vacancy (Frenkel defect) or at infinite distance (hole vacancy). E_{Fr} in the Li_2O (111) surface is 151 kJ mol^{-1} , considerably smaller than the measured bulk value (244 kJ mol^{-1} [34]). Therefore, it was concluded [15] that the defect concentration is higher in the surface than in the bulk which plays a major role for Li diffusion.

6.2.3. Li^+ migration. In a previous theoretical work [35], it has been shown that the migration barrier of the Li interstitialcy mechanism is higher than that of the vacancy mechanism. This was supported by more recent

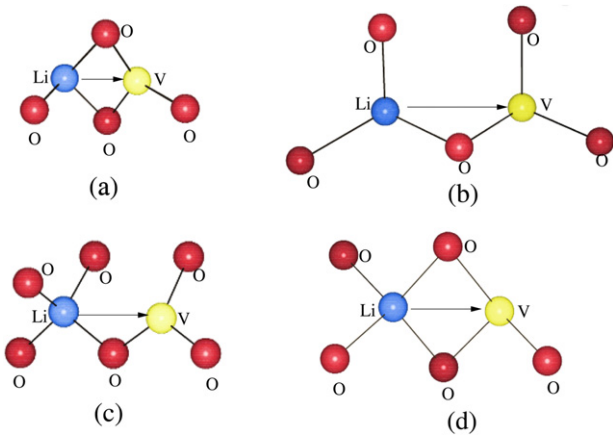


Figure 6. Schematic representation of possible Li hopping processes: (a), (b) a three-fold coordinated Li^+ ion (first layer) migrates to a three-fold coordinated vacancy site; (c), (d) a four-fold coordinated Li^+ ion (third layer) migrates to a three-fold coordinated vacancy site.

experimental investigations on the Li^+ migration in Li_2O [1], where a vacancy mechanism was proposed. Therefore, we concentrated on the vacancy mechanism in our subsequent investigation of Li diffusion in Li_2O [15]. A 4×4 supercell with six atomic layers was employed for the investigation of Li^+ migration in the $\text{Li}_2\text{O}(111)$ surface. In the previous section, it was observed that the basis set has a very small effect on both cation vacancy and Frenkel defect formation energy values. Therefore, only the smaller BS A was applied for the Li^+ migration investigation.

As a first step, a single neutral Li atom was removed from the Li_2O slab. This is a simplification of the real situation where Li remains in the lattice and may affect the movement of other Li atoms. But in the present investigation we are interested only in the activation barriers for hopping processes between regular lattice sites. Li migration may then occur from a tetrahedral third-layer site to a cation vacancy at the top-most layer which is only three-fold coordinated to oxygen atoms, or vice versa. Another possibility is a hopping process between an occupied and an unoccupied three-fold coordinated site of the first layer. In both cases, one or two oxygen atoms are shared by the migrating Li^+ and the cation vacancy as shown in figure 6.

We assumed in [15] that the transition state is located in the middle of the path between the initial position of the migrating atom and the vacancy. This represents an approximation of the real transition state that might deviate from the central position due to the reduced symmetry at the surface. Unfortunately, a full transition state search was not possible with CRYSTAL06 at that time. The possibility of a different migration path such as Li^+ ion movement in a two-dimensional curve rotation was investigated in a previous study [10]. There it was observed that, for the Li^+ ion migration in crystalline Li_2O , the activation energy E_A in the curve rotation is almost identical to that obtained in the straight line path. Therefore we are convinced that the conclusions of our study are not affected by the limited accuracy of the transition state geometries. In the following,

Table 13. Comparison of calculated Li^+ migration energies E_A (eV) in the $\text{Li}_2\text{O}(111)$ surface with those in bulk Li_2O . (Method: PW1PW, basis set (BS): A.)

a b	$\text{Li}_2\text{O}(111)$ surface				Li_2O bulk	
	A1				Exp. [1]	Calc. [10]
$E_A(ab)$	0.25	1.10	1.16	1.02	0.31	0.33
$E_A(ba)$	0.08	0.89	1.11	1.02		

we describe the possible pathways for Li^+ migration in the Li_2O surface.

In figure 5, selected lithium atoms are denoted to represent the possible migration pathways for the Li^+ ion movement. Li A1 and Li E are nearest neighbours in the first atomic Li layer, B1 and C are in the third atomic layer, and D belongs to the next Li row of the first layer. The migration of a Li^+ ion can occur in a zig-zag pathway, such as the migration of lithium type A1 to B1, or A1 to C. Alternatively, migration can occur in a straight line, either along the $[\bar{1}10]$ -direction via $A1 \rightarrow D$ or along the $[\bar{1}\bar{1}0]$ -direction ($A1 \rightarrow E$).

Spin polarization plays an important role for the Li^+ migration. It was observed that the unpaired electron, created due to the cation vacancy, is localized on the 2p orbital of one of the surrounding oxygen atoms. For the migration of A1 to B1 and A1 to C, spin is localized on the oxygen atom nearer to the migrating lithium in the transition states, whereas in the case of A1 to D and A1 to E migrations, the unpaired electron is localized on the oxygen atom nearer to the defect in the transition states. A similar situation was observed for Li^+ diffusion in crystalline Li_2O [10] (see section 6.1.3).

The calculated values for the migration energy E_A for all considered migration pathways are presented in table 13. Unlike in the case of bulk Li_2O , the migration energy E_A for the Li ion migration in the Li_2O surface is not symmetric because the sites are not energetically equivalent. We therefore distinguished between $E_A(ab)$ and $E_A(ba)$ where the energy of the transition state refers to the structure with occupied site a (b) and empty site b (a).

The zig-zag migrations are more suitable than the migrations in the straight lines along either the $[\bar{1}10]$ -direction or the $[\bar{1}\bar{1}0]$ -direction. The smallest activation barriers were found for the migration of lithium type A1 to B1 along the zig-zag pathway. For the $A1 \rightarrow B1$ direction E_A is 0.25 eV. The experimental values are 0.31 eV (Li_2O bulk [1]), 0.34 ± 0.04 eV ($\text{Li}_2\text{O}:\text{B}_2\text{O}_3$ nanocomposite [3]) and 0.30 ± 0.02 eV ($\text{Li}_2\text{O}:\text{Al}_2\text{O}_3$ nanocomposite [6]). For the hopping process in the opposite direction $B1 \rightarrow A1$ E_A is much smaller, 0.08 eV (table 13) due to the higher energy of a Li vacancy at site B1 compared to A1.

In a macroscopic process where Li vacancies migrate over distances corresponding to many lattice parameters, both barriers have to be overcome. The smaller barrier, corresponding to the fast step, will not be observed in the experiments.

According to our present results, the migration energy barriers in the bulk and surface of Li_2O are not significantly different. The increased Li mobility near grain boundaries of

Table 14. Formation energy of a Li defect $E_{\text{de}}(\text{V})$ (kJ mol^{-1}) in $\alpha\text{-LiBO}_2$ as a function of the defect concentration c (%), unrel = unrelaxed, rel = relaxed [12].

Supercell	c	PW1PW		PW91–PAW	
		Unrel	Rel	Unrel	Rel
$\text{Li}_4\text{B}_4\text{O}_8$	6.25	709	701	677	663
$\text{Li}_{32}\text{B}_{32}\text{O}_{64}$	0.78	717	698	678	667
$\text{Li}_{108}\text{B}_{108}\text{O}_{216}$	0.23			702	673

nanocrystallites is therefore attributed mainly to the increased Li vacancy concentration due to their higher thermodynamical stability compared to the bulk. This is in agreement with the experimental results [1, 5, 6].

7. Defects and diffusion in LiBO_2 bulk

Due to the fast ionic conduction property, lithium metaborate has a number of potential applications in advanced materials with controlled chemical and new physical properties such as lithium ion batteries, electrochromic displays, gas sensors, etc [1, 72, 134]. Recently, experimental studies on ion transport and diffusion in nanocrystalline and glassy ceramics of LiNbO_3 , $\text{LiAlSi}_2\text{O}_6$ and LiBO_2 using the measurement of dc conductivities and ^7Li nuclear magnetic resonance spin–lattice relaxation rates have been performed [72, 73]. Their measured activation energy for the Li^+ ion long-range transport as derived from the dc conductivity in LiBO_2 (with $\alpha\text{-LiBO}_2$ as the majority phase) is 0.80–0.71 eV when going from the microcrystalline via the nanocrystalline to the glassy state, whereas the activation energy for the short-range Li^+ ion migration obtained from the spin–lattice relaxation rates is 0.23–0.21 eV when going from the nanocrystalline to the glassy state. Based on these values, the experimental activation energy for short-range Li^+ ion migration in the microcrystalline state is estimated to be 0.30 eV.

Here, we review a theoretical investigation of the Li vacancy defect and the migration of a Li^+ ion in $\alpha\text{-LiBO}_2$ using first-principles methods and periodic supercell models [12]. Calculations with LCAO based approaches were performed with basis set B (BS B), whereas plane wave based calculations were performed with energy cutoff $E_{\text{cut}} = E_2$.

7.1. Cation vacancy in LiBO_2

The formation energy of a cation vacancy $E_{\text{de}}(\text{V})$ is calculated with equation (2) for unrelaxed and fully relaxed systems. Supercells ($\text{Li}_4\text{B}_4\text{O}_8$, $\text{Li}_{32}\text{B}_{32}\text{O}_{64}$ and $\text{Li}_{108}\text{B}_{108}\text{O}_{216}$) were used for defect calculations. The lowest vacancy concentration that we studied here was therefore 0.23%. In table 14, calculated cation vacancy formation energies are presented only for the PW1PW and PW91–PAW approaches.

To the best of our knowledge there is no previous experimental or theoretical value for the Li vacancy formation energy of LiBO_2 . Therefore the calculated $E_{\text{de}}(\text{V})$ values obtained with different methods are compared with each other

in the following. Since PW1PW gives the best reproduction of the experimental bulk and defect properties of Li_2O [10] and $\text{Li}_2\text{B}_4\text{O}_7$ [14, 17], this method is taken as internal reference. $E_{\text{de}}(\text{V})$ for the fully relaxed system obtained with PW1PW is 698 kJ mol^{-1} . As for the Li vacancy defect in Li_2O [10] and $\text{Li}_2\text{B}_4\text{O}_7$ [17], the pure DFT approach PW91–PAW gives a smaller value of $E_{\text{de}}(\text{V})$ (673 kJ mol^{-1}) compared to PW1PW. But, in general, there is close agreement between the various theoretical approaches indicating that the effects of self-interaction in GGA-DFT and of basis set limitation in the LCAO based method are not significant.

The relaxation energies E_{R} , 19–29 kJ mol^{-1} , are of the order of 3–5% of the defect formation energies. The absolute values of E_{R} are smaller than those obtained for Li_2O [10] and $\text{Li}_2\text{B}_4\text{O}_7$ [17], indicating less relaxation effect on the defect formation in LiBO_2 . Here it should be noted that employment of the largest supercell $\text{Li}_{108}\text{B}_{108}\text{O}_{216}$ with the LCAO based PW1PW method was not possible due to the huge CPU time requirement. However, the calculated $E_{\text{de}}(\text{V})$ has already converged with the medium sized supercell $\text{Li}_{32}\text{B}_{32}\text{O}_{64}$ within 3–4 kJ mol^{-1} with all the methods.

The effect of relaxation is further investigated by measuring the changes of distances of the nearest oxygen atoms, boron atoms and lithium atoms with respect to the defect position during geometry optimization. In non-defective LiBO_2 , the Li atom is surrounded by four oxygen atoms in a distorted tetrahedral arrangement [124]. The four lithium–oxygen distances range from 1.93 to 2.00 Å [124]. Thereupon follows a fifth lithium–oxygen distance of 2.52 Å, forming an oxygen five-vertex polyhedron [124]. In the following the five nearest oxygen atoms are considered to show the effect of relaxation. The three nearest boron atoms (B1, B2 and B3) and two nearest lithium atoms (Li1 and Li2) to the vacancy are also considered. The numbering follows that in figure 7. In table 15, the calculated distances of the O, B and Li atoms from the vacancy before and after relaxation are shown. Here r_1 to r_{10} denote the distances of the O, B and Li atoms from the vacancy. The numbering follows that in figure 7.

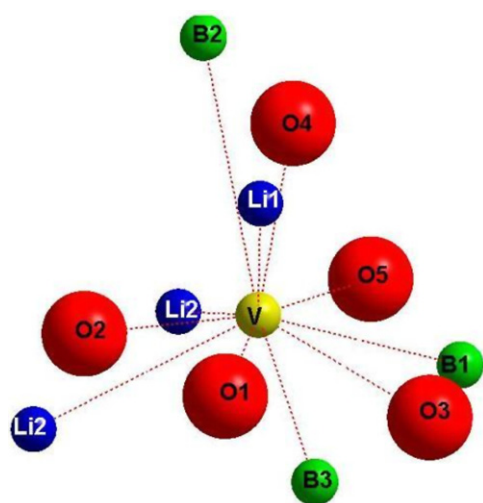
With both methods an increase of the nearest-neighbour oxygen-defect position distance is obtained. This is due to the fact that the electrostatic attraction by the Li^+ ion is missing. The fifth oxygen atom shows only a small relaxation, +0.2% (PW1PW), or +0.4% (PW91–PAW), indicating that relaxation is mainly restricted to the nearest neighbours of the vacancy. All the boron atoms move towards the vacancy by a very small amount. Also the two nearest lithium atoms show an inward relaxation. This behaviour can be explained by the reduced electrostatic repulsion of the positively charged boron and lithium ions after removal of a Li atom. The movement of the nearest Li neighbours around the vacancy in LiBO_2 is in line with the corresponding geometry changes in Li_{2-x}O [10] and $\text{Li}_{2-x}\text{B}_4\text{O}_7$ [17], where the nearest Li atoms show strong inward relaxation.

7.2. Electronic properties

The removal of a neutral Li atom creates a hole in the valence band. One of the surrounding oxygen atoms which

Table 15. Distances r (Å) of the nearest oxygen, boron and lithium atoms in α -LiBO₂ from the Li vacancy (V) and changes Δr of the distances (in % of r) due to relaxation [12].

Distance	Vacancy–atom	PW1PW			PW91–PAW		
		Unrelaxed	Relaxed	Δr (%)	Unrelaxed	Relaxed	Δr (%)
r_1	V–O1	1.933	1.947	+0.72	1.961	2.002	+2.09
r_2	V–O2	1.939	1.963	+1.24	1.963	2.006	+2.20
r_3	V–O3	1.983	2.019	+1.82	1.997	2.030	+1.65
r_4	V–O4	1.999	2.023	+1.20	2.019	2.050	+1.55
r_5	V–O5	2.518	2.522	+0.15	2.510	2.521	+0.42
r_6	V–B1	2.636	2.617	−0.73	2.645	2.637	−0.30
r_7	V–B2	2.751	2.739	−0.44	2.986	2.934	−1.74
r_8	V–B3	2.860	2.851	−0.31	2.878	2.857	−0.73
r_9	V–Li1	2.589	2.503	+3.32	2.623	2.504	−4.54
r_{10}	V–Li2	2.773	2.745	−1.01	2.798	2.668	−4.65

**Figure 7.** Nearest oxygen, boron and lithium atoms to the Li vacancy (V) in α -LiBO₂ crystal. The blue, green, red and yellow spheres represent lithium, boron, oxygen and the Li vacancy respectively [12]. Reproduced with permission from [12]. Copyright 2011 American Chemical Society.

was formally O^{2−} in stoichiometric LiBO₂ becomes O[−]. One unpaired electron is localized on the 2p orbital of one of those oxygen atoms.

The study of electronic properties is performed by calculating the density of states (DOS) of the defective supercells. The DOS for a defective Li₃₂B₃₂O₆₄ supercell obtained with PW1PW is shown in figure 8. Pure DFT approaches show qualitatively the same behaviour. The main difference of DFT-GGA approaches (such as PW91–PAW) from PW1PW is that the energetic difference between occupied and unoccupied bands is smaller for the PW91–PAW method. The Li⁺ vacancy introduces an extra unoccupied level 1.0 eV above the Fermi level E_F , which is marked in figure 8. With PW91–PAW, this energy difference is 0.40 eV.

This band is mainly composed of oxygen p orbitals from atoms surrounding the vacancy site. In the analysis of the electronic structure obtained with PW1PW it is found that the p orbitals of one of the four nearest oxygen atoms have much larger contributions than those of the other atoms. This corresponds to the simplified picture of a change from O^{2−} to O[−] for a single ion, whereas with plane wave based

PW91–PAW the contributions to the defect band are more evenly distributed, therefore the hole is less localized.

7.3. Migration of a Li⁺ ion

In our previous study of the Li⁺ ion migration in Li₂O (see section 6.2.3 [10]), it was observed that both the hybrid and pure DFT approaches give similar agreement with respect to the experimental values. Since the NEB method has not yet been implemented in CRYSTAL, we have only employed the VASP PW91–PAW approach for calculating the Li ion migration in LiBO₂. There are various possibilities for Li⁺ migration in LiBO₂ as presented in figure 9. Li⁺ can migrate along the xy plane, such as (a) migration of Li A to Li B1 (distance 2.623 Å), (b) migration of Li A to Li B2 (distance 2.798 Å), (c) migration of Li A to Li B3 (distance 2.798 Å) and (d) migration of Li A to Li B4 (distance 3.120 Å). Another possibility for Li⁺ migration is in the c direction indicated by positions A and C in figure 9. In this case the distance between two lithium atoms is 3.314 Å.

The structural analysis of the migration pathways along the xy plane and the c direction shows that there are clear differences among the neighbouring sites of migrating lithium and vacancy positions. Compared to the migration along the c direction, the distance between the migrating Li and the Li vacancy is shorter for the migrations along the xy plane. In the latter case, two oxygen atoms are bridging between the migrating Li and the Li vacancy, whereas for the migration along the c direction, one oxygen atom is bridging between the migrating Li and the Li vacancy.

For simplicity, here we present the local structures of only one migration pathway along the xy plane (migration of Li A to Li B1) in figure 10 and compare these with the local structures of migration along the c direction (migration of Li A to Li C) in figure 11. As discussed in section 7.1, the lithium atom (or lithium vacancy as marked by V in figures 10 and 11) is surrounded by five oxygen atoms as nearest neighbours O1 (O1), O2 (O2), O3 (O3), O4 (O4) and O5 (O5). In the case of migration along the xy plane, the migrating Li (blue sphere in figure 10) is in the middle of two bridging oxygen atoms in the transition state structure. In the final structure, the distance between the migrating Li and the O atoms has increased slightly ($\Delta d = +0.10$ to $+0.20$ Å) due to structural

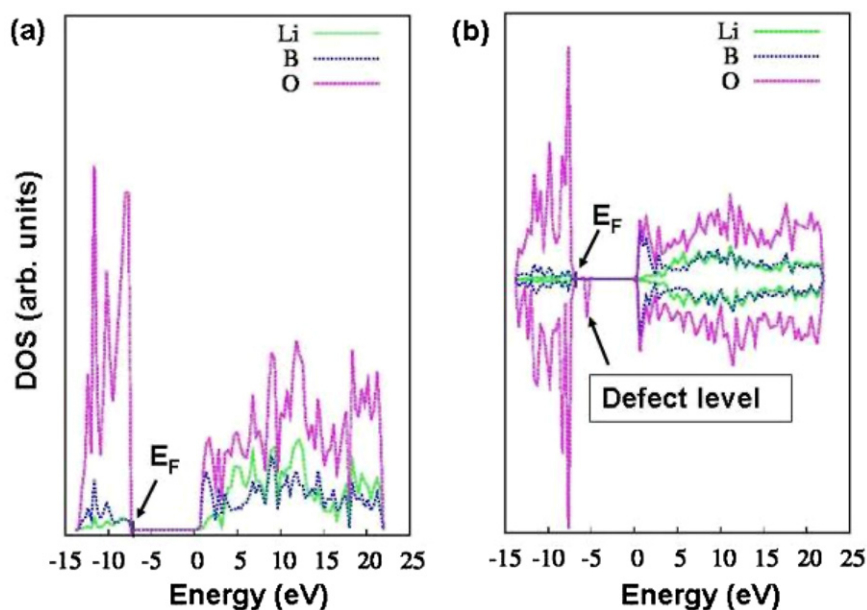


Figure 8. Density of states (DOS) for stoichiometric and Li defective $\text{Li}_{32}\text{B}_{32}\text{O}_{64}$ supercells obtained with PW1PW. E_F denotes the Fermi level [12]. Reproduced with permission from [12]. Copyright 2011 American Chemical Society.

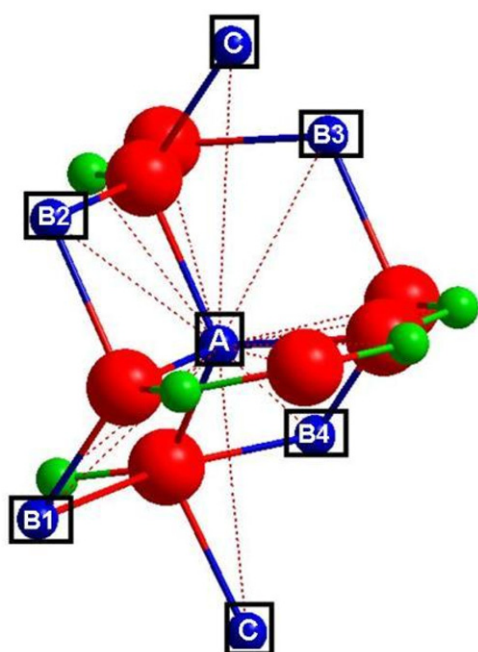


Figure 9. Local structure showing various migration pathways containing a Li point defect in LiBO_2 . The blue, red and green spheres represent Li, O and B, respectively [12]. Reproduced with permission from [12]. Copyright 2011 American Chemical Society.

relaxation. For the Li^+ ion migration along the c direction, the migrating Li (blue sphere in figure 11) passes through a triangle formed by three oxygen atoms. Here the three Li–O distances are 1.83, 1.93 and 2.18 Å. Due to strong relaxation, the Li–O distance has increased ($\Delta d = +0.34$ Å).

The investigation of all the structures in the migration pathways reveals that the unpaired electron is localized on the p orbitals of the nearest oxygen atoms. As stated before, the contributions to the defect band are more evenly distributed

Table 16. Comparison of calculated activation energy E_A (eV) values in $\alpha\text{-LiBO}_2$ with experimental results [12].

Migration type	Calc.	Exp. [72, 73]
A–B1	0.43	
A–B2(B3)	0.43	
A–B4	0.54	
A–C	0.55	
		0.21–0.23, 0.30, 0.71–0.80

with the plane wave based PW91–PAW method. Therefore the hole is less localized. The same situation was observed in our previous studies of Li^+ migration in Li_2O [10, 15].

As in the case of Li_2O [10], the migration path is symmetric as the initial and final positions in the migration pathway are energetically equivalent. In table 16, the calculated activation energies (E_A) are compared with the experimental values [72, 73].

Our calculated E_A in the xy plane ranges between 0.43 and 0.54 eV whereas that along the c direction is 0.55 eV. This shows that the migration of a Li^+ ion along the xy plane would be easier than that in the c direction. The calculated E_A (0.43–0.55 eV) is in the range of experimental E_A values for $\alpha\text{-LiBO}_2$ (0.21–0.23 eV, 0.30 eV and 0.71–0.80 eV) [72, 73].

8. Defects and diffusion in $\text{Li}_2\text{B}_4\text{O}_7$ bulk

The main structural pattern of lithium tetraborate (LTB) is a $[\text{B}_4\text{O}_9]^{6-}$ complex which consists of two planar trigonal (BO_3) and two tetrahedral (BO_4) units. Lithium ions are connected with the anion subsystem electrostatically [128]. The loose connectivity results in the appearance of ionic conductivity and superionic properties [61]. Experimental investigations [135, 136] of the temperature dependence

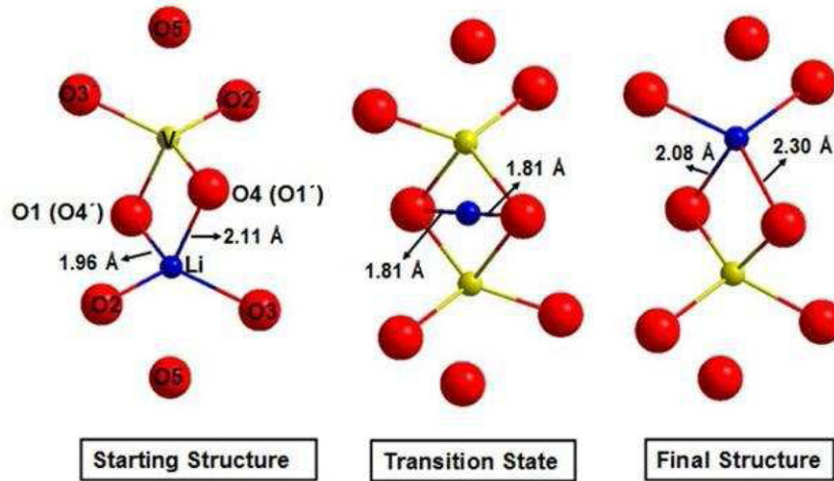


Figure 10. Local structures for the Li^+ ion migration in LiBO_2 along the xy plane, where in the starting structure two oxygen atoms are bridging between the migrating Li (blue sphere) and the Li vacancy (yellow sphere, marked with V). In the transition state the migrating Li passes through two bridging oxygen atoms [12]. Reproduced with permission from [12]. Copyright 2011 American Chemical Society.

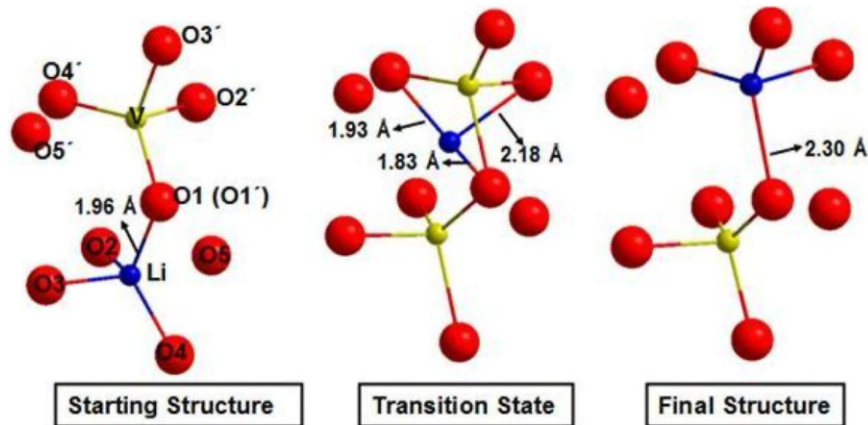


Figure 11. Local structures for the Li^+ ion migration in LiBO_2 along the c plane, where in the starting structure one oxygen atom is bridging between the migrating Li (blue sphere) and the Li vacancy (yellow sphere, marked with V). In the transition state the migrating Li passes through a triangle formed by three oxygen atoms [12]. Reproduced with permission from [12]. Copyright 2011 American Chemical Society.

of conductivity for LTB single crystals showed that the conductivity along the tetragonal c axis is higher by almost five orders of magnitude than that along the perpendicular direction. In these studies it was established that the conductivity of LTB crystals is purely electronic along the (100) direction and purely ionic (via transport of Li ions) along the (001) direction. Since then, several experimental investigations have been performed to study the ionic conductivity of this system along the (001) direction [92–97]. It was suggested [94] that the conduction of the Li^+ ion occurs through a one-dimensional channel in the tetragonal axis. This conductivity channel is formed by the triangular faces of the five-vertex oxygen polyhedra around the main lithium position. The ionic conductivity in LTB is attributed to the Li vacancies [92–94].

Several different values for the activation energy E_A of the ion migration in LTB exist in the literature. They are dependent on the preparation method of the samples [94]. Kim

et al [93] measured the E_A for LTB crystals prepared from LTB powder (LTBp, 0.42 eV) and from $\text{Li}_2\text{CO}_3\text{--B}_2\text{O}_3$ mixed powder (LTBm, 0.46 eV).

In the following, we review our theoretical investigation of the Li vacancy defect and the migration of a Li^+ ion in LTB [17]. Calculations with LCAO based approach were performed with basis set B (BS B), whereas plane wave based calculations were performed with energy cutoff $E_{\text{cut}} = E_2$.

8.1. Cation vacancy in lithium tetraborate

For the simulation of a Li vacancy in LTB, a supercell $\text{Li}_{16}\text{B}_{32}\text{O}_{56}$ was created by applying the transformation matrix \mathbf{L} on the primitive unit cell:

$$\mathbf{L} = \begin{pmatrix} 0 & 1 & 1 \\ 1 & 0 & 1 \\ 1 & 1 & 0 \end{pmatrix}. \quad (5)$$

Table 17. Effect of relaxation on the formation energy of a single Li vacancy, $E_{\text{de}}(\text{V})$ (kJ mol^{-1}), in $\text{Li}_2\text{B}_4\text{O}_7$ [17].

	Unrelaxed	Relaxed
PW1PW	800	728
PW91–PAW	693	658

This supercell corresponds to the conventional unit cell of LTB and contains 104 atoms. A full optimization of atomic fractional coordinates was performed taking the optimized lattice parameters ($a = 9.50 \text{ \AA}$ and $b = 10.32 \text{ \AA}$) from the bulk optimization [14].

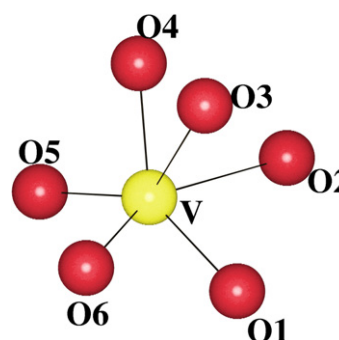
The formation energies for a cation vacancy, $E_{\text{de}}(\text{V})$, are calculated with equation (2) for unrelaxed and fully relaxed systems, and are presented in table 17. To the best of our knowledge there is no previous experimental or theoretical value for the Li vacancy formation energy of LTB. Therefore the calculated $E_{\text{de}}(\text{V})$ values obtained with PW1PW and PW91–PAW are compared with each other in the following. Since PW1PW gives the best reproduction of the experimental bulk properties of LTB [14] and of the defect properties of Li_2O [10] and LiBO_2 [12], this method is taken as reference. The $E_{\text{de}}(\text{V})$ for the fully relaxed system obtained with PW1PW is 728 kJ mol^{-1} .

As for the Li vacancy defect in Li_2O , the PW91–PAW approach gives a significantly smaller value of $E_{\text{de}}(\text{V})$ (658 kJ mol^{-1}) compared to PW1PW. The absolute values for the Li defect formation energy are considerably higher in LTB than in Li_2O . There we obtained 576 kJ mol^{-1} (PW1PW) and 480 kJ mol^{-1} (PW91–PAW). In part this can be explained by the larger bandgap in LTB (9.3 eV , [13, 14]) compared to Li_2O (8.0 eV , PW1PW [10]). For both systems the top of the valence band is dominated by O 2p levels whereas the lower part of the conduction band consists mainly of Li 2sp orbitals (Li_2O), or Li 2sp and B 2sp orbitals (LTB), respectively [13]. Therefore the reduction of an oxygen atom after removal of a Li atom is energetically less costly in the system with the smaller bandgap.

For a more quantitative analysis we compared the Mulliken overlap population of Li with its neighbours in LTB and Li_2O . Surprisingly, the overlap population with the four nearest oxygen neighbours is larger in Li_2O (0.043) than in LTB (average value 0.015). This would indicate a weaker Li–O bond in LTB in contrast to the calculated defect formation energies. But in LTB the overlap population decays very slowly. Second nearest O and B atoms still have overlap populations of 0.011 with the Li atom. This indicates a more covalent nature of the bond in LTB which can explain the larger $E_{\text{de}}(\text{V})$. In Li_2O all overlap populations are zero except for the nearest neighbours.

The relaxation energies E_{R} , 72 kJ mol^{-1} with PW1PW and 35 kJ mol^{-1} with PW91–PAW, obtained for LTB are of the order of 6–10% of the defect formation energies. The absolute values of E_{R} are larger in LTB than those obtained for Li_2O [10].

The effect of relaxation is further investigated by measuring the changes of distances of the nearest oxygen atoms, boron atoms and lithium atoms with respect

**Figure 12.** The six nearest oxygen atoms to the Li vacancy (V) in $\text{Li}_2\text{B}_4\text{O}_7$ crystal [17].**Table 18.** Calculated values of changes in distances of the nearest oxygen atoms to the Li vacancy (V), Δr (in % of r), due to relaxation in $\text{Li}_2\text{B}_4\text{O}_7$ [17].

Distance	Vacancy–atom	PW1PW (Δr) (%)	PW91–PAW (Δr) (%)
r_1	V–O1	+4.1	+3.0
r_2	V–O2	+5.0	+4.0
r_3	V–O3	+2.4	+2.9
r_4	V–O4	+4.3	+1.9
r_5	V–O5	+4.4	+7.6
r_6	V–O6	+0.2	+0.4

to the defect position during geometry optimization. In non-defective LTB, the Li atom is surrounded by four oxygen atoms in a distorted tetrahedral arrangement [128, 137]. The four lithium–oxygen distances range from 1.97 to 2.17 \AA [128]. The next shell follows a fifth lithium–oxygen distance of 2.61 \AA , forming an oxygen five-vertex polyhedron [94, 128]. The next lithium–oxygen distances are 2.85 \AA and more. In the following the six nearest oxygen atoms are considered to show the effect of relaxation (figure 12). In table 18, the calculated values of changes in distances (r) of O atoms Δr are shown.

Here r_1 to r_6 denote the distances of O1–O6 from the vacancy. The numbering follows that in figure 12. With both methods an increase of the oxygen–defect position distance is obtained. This is due to the fact that the electrostatic attraction by the Li^+ ion is missing. The removal of a neutral Li atom creates a hole in the valence band. One of the surrounding oxygen atoms which was formally O^{2-} in stoichiometric LTB becomes O^- . One unpaired electron is localized on the 2p orbital of one of these oxygen atoms. It should be noted that the sixth oxygen atom shows a small relaxation, +0.2% (PW1PW) or +0.4% (PW91–PAW), indicating that relaxation is mainly restricted to the nearest neighbours of the vacancy.

The calculated changes in distances of the three nearest boron atoms and two nearest lithium atoms from the vacancy due to relaxation are shown in table 19.

r_1 , r_2 and r_3 denote the distances of the three boron atoms, respectively, and r_4 denotes the distance of the two lithium atoms from the vacancy. Two of the boron atoms move towards the vacancy, while the position of the third boron atom is unchanged with both methods, $\Delta r = 0.0\%$ (PW1PW) and -0.2% (PW91–PAW). Also the two nearest lithium atoms

Table 19. Calculated changes in distances, Δr (in % of r), of the nearest boron and lithium atoms from the Li vacancy (V) due to relaxation in $\text{Li}_2\text{B}_4\text{O}_7$ [17].

Distance	Vacancy–atom	PW1PW (Δr)	PW91–PAW (Δr)
r_1	V–B1	–0.4	–0.8
r_2	V–B2	–0.7	–1.1
r_3	V–B3	–0.0	–0.2
r_4	V–Li	–4.2	–2.9

show an inward relaxation of -4.2% with the PW1PW and -2.9% with the PW91–PAW approach. This behaviour can be explained by the reduced electrostatic repulsion of the positively charged boron and lithium ions after removal of a Li. The movement of the nearest Li neighbours around the vacancy in LTB is in line with the corresponding geometry changes in Li_{2-x}O [10], where the nearest Li atoms show strong inward relaxation.

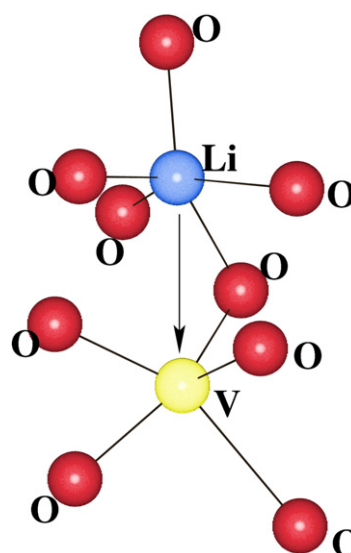
The study of electronic properties is performed by calculating the density of states (DOS) of the defective supercells. The main difference between PW91–PAW and PW1PW is that the energetic difference between occupied and unoccupied bands is smaller with PW91–PAW due to the self-interaction error. The Li^+ vacancy introduces an extra unoccupied level 0.26 eV above the Fermi level E_F with the PW1PW approach.

With PW91–PAW this energy difference is virtually identical, 0.27 eV. This band is mainly composed of oxygen p orbitals from atoms surrounding the vacancy site. In the analysis of the electronic structure obtained with PW1PW it is found that the p orbitals of one of the four nearest oxygen atoms have much larger contributions than those of the other atoms. This corresponds to the simplified picture of a change from O^{2-} to O^- for a single atom. With PW91–PAW, the contributions to the defect band are more evenly distributed, therefore the hole is less localized. Again, this has to be attributed to the inherent self-interaction error in GGA–DFT. In this aspect, hybrid methods are more reliable. Nevertheless, the effect of localization on calculated defect formation energy and activation energy barriers is relatively small.

8.2. Migration of a Li^+ ion

In LTB, a Li^+ ion migrates through a one-dimensional channel of the ion conduction path in the (001) direction [94]. In this channel, Li ions form five-vertex oxygen polyhedra (LiO_5). The high atomic packing density and the rigidity of the triangular and tetrahedral boron–oxygen polyhedra prevent direct jumps of Li ions along the tetragonal axis [94]. It is assumed that the Li^+ ion migrates through the large triangular faces of the two nearest oxygen five-vertex polyhedra facing each other. In figure 13, two nearest oxygen five-vertex polyhedra, one of a Li ion and the other of an adjacent Li vacancy (V), are shown. The arrow shows the direction of the migrating Li^+ ion towards the vacancy.

Two schematic views of the Li^+ ion migration process in LTB are presented in figures 14 and 15. Here it should be

**Figure 13.** The two nearest oxygen five-vertex polyhedra of the lithium and the vacancy (V) along the tetragonal axis of $\text{Li}_2\text{B}_4\text{O}_7$ crystal.

noted that the migration pathways were designed manually and the energetics of each step of the migration were calculated separately as the cNEB method was not available at that time. In the following we discuss the migration pathways. The migrating Li^+ ion and the vacancy V are in their original positions in figures 14(a) and 15(a). The migration path is modelled in four steps. In step I (figures 14(b) and 15(b)) one Li^+ ion migrates to the adjacent vacancy. The migrating Li^+ ion accesses the position of the vacancy and the vacancy is created at the original position of the migrating ion. Similarly, in the following steps II–IV (figures 14(c)–(e) and 15(c)–(e)), the Li^+ ion migrates along the (001) direction.

The calculated values of the Li hopping distance are 3.06 Å and 3.08 Å with PW1PW and PW91–PAW respectively, in good agreement with the experimental hopping distance of 3 Å [94]. In figure 16, the potential energy curves for the Li^+ ion migration in LTB for unrelaxed systems are shown.

In each step, the migration path is modelled in ten sub-steps. The central sub-step is considered as an approximation of the corresponding transition structure. The activation energy E_A is calculated (for both the unrelaxed and relaxed systems) as the energy difference of the approximate transition structure and the initial structure where the vacancy is on a regular site. In table 20, the calculated activation energies are compared with the experimental values [93]. For every step E_A is the same, reflecting that the local environments of the migrating Li^+ ion and the vacancy are identical. Therefore, only one step is shown in figures 16 and 17. For the unrelaxed system, both the PW1PW and the PW91–PAW method give too large values (1.87 eV and 2.22 eV respectively) for E_A compared to experiment (0.42–0.46 eV, table 20). This is in line with the previous finding for Li^+ ion diffusion in Li_2O [10] and demonstrates the high importance of local relaxation for the calculation of activation barriers. The potential energy curves for Li^+ ion migration for the fully relaxed systems are shown in figure 17.

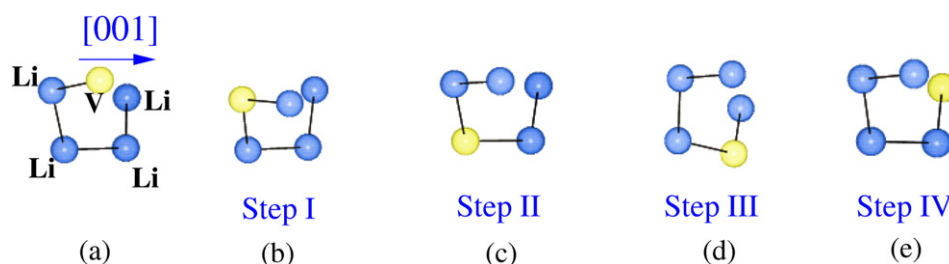


Figure 14. Schematic representation of the Li⁺ ion migration in Li₂B₄O₇ (top view).

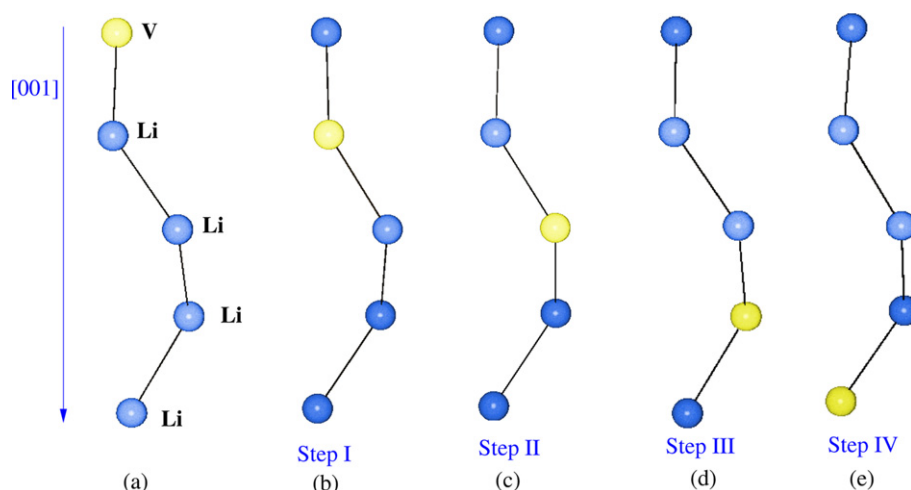


Figure 15. Schematic representation of the Li⁺ ion migration in Li₂B₄O₇ (side view).

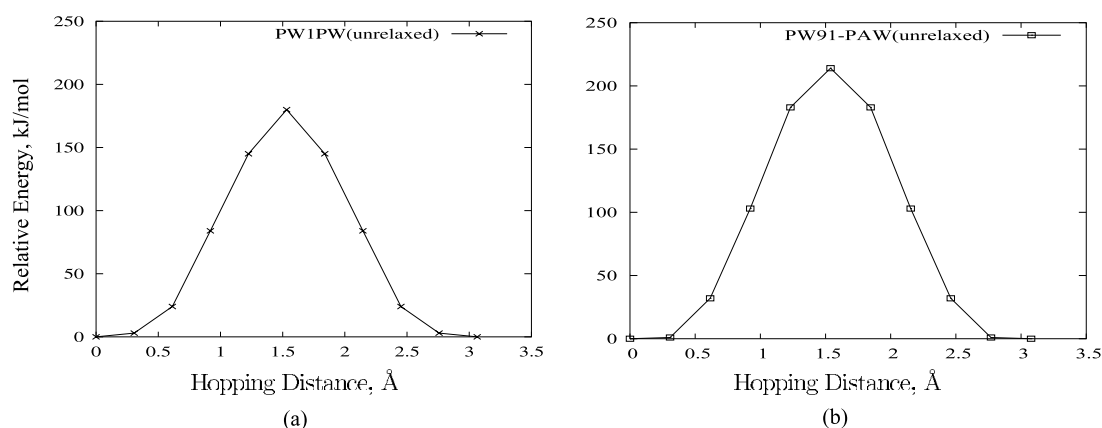


Figure 16. Potential energy curves for Li⁺ ion migration in Li₂B₄O₇ without relaxation: (a) PW1PW and (b) PW91-PAW. Reproduced with permission from [17]. Copyright 2006 American Chemical Society.

Both methods, PW1PW (0.37 eV) and PW91-PAW (0.27 eV), now give good agreement with the experimental activation energies. As for Li₂O [10], the PW1PW value better agrees with the experimental activation energy for LTB, deviating by only 0.05 eV.

9. Defects and diffusion in Li₂O:B₂O₃ nanocomposites

This study was motivated by recent experiments, where it has been observed that the diffusivity in Li₂O:B₂O₃ [1–3] and Li₂O:Al₂O₃ nanocomposites [6] is higher than in

Table 20. Comparison of calculated activation energies, E_A (eV), in Li₂B₄O₇ with and without relaxation with experimental values [17].

Method	Unrelaxed	Relaxed
PW1PW	1.87	0.37
PW91-PAW	2.22	0.27
Exp. [93]		0.42, 0.46

nanocrystalline Li₂O, although B₂O₃ and Al₂O₃ are insulators. This surprising effect was attributed to the increased fraction of structurally disordered interfacial regions in nanocomposite materials [1]. Several classical

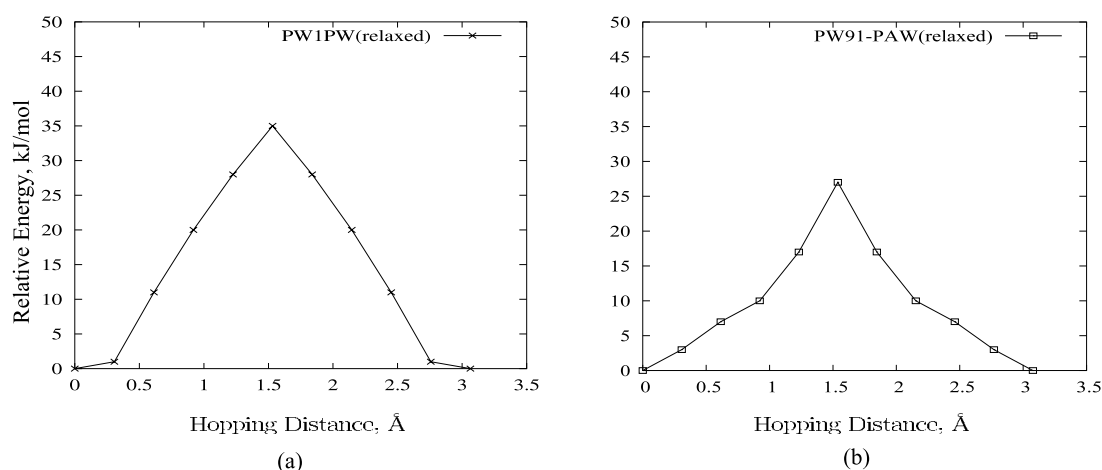


Figure 17. Potential energy curves for Li⁺ ion migration in Li₂B₄O₇ with relaxation: (a) PW1PW and (b) PW91-PAW. Reproduced with permission from [17]. Copyright 2006 American Chemical Society.

models have been employed to describe the enhanced ionic conductivity in composite materials. The continuum percolation model was used to describe the dependence of the dc conductivity of Li₂O:B₂O₃ nanocrystalline composites on the insulator concentration [2]. A brick-layer type percolation model treating both the micro- and nanocrystalline composites on the same footing [4] is also able to reproduce the experimental results for the conductivity as a function of composition. In a recent investigation [5], a more sophisticated Voronoi approach was used. None of these stochastic models explicitly take into account the structure of the nanoparticles and of their surfaces.

For the first time, we have developed atomistic models of the Li₂O:B₂O₃ nanocomposite based on periodic slabs [9]. The effect of the atomic structure in the interface region on the ion mobility was investigated. The enhancement of Li conductivity in the Li₂O:B₂O₃ interface region was investigated by the calculation of defect concentration and activation barriers for local hopping processes in the interfacial region. Calculations were performed with the PW1PW method using BS A.

9.1. Structural models

We have modelled the Li₂O:B₂O₃ nanocomposite as a combination of the energetically favourable Li₂O(111) surface (see section 5.1) [15, 131] and the most commensurate B₂O₃(001) surface (see section 5.2) [16]. A 4 × 4 supercell of the primitive Li₂O(111) surface unit cell was used as the model for the Li₂O surface [15]. The lengths of the corresponding surface lattice vectors were $a = b = 12.9$ Å. The B₂O₃(001) surface was modelled with a 3 × 3 supercell [16] with surface lattice parameters $a = b = 13.1$ Å. The slab model had five atomic layers and contained 9 f.u. The surface lattice parameters were $a = b = 13.1$ Å, corresponding to the optimized bulk structure at PW1PW level, $a_{\text{bulk}} = 4.35$ (exp. 4.34) Å, $c_{\text{bulk}} = 8.39$ (8.34) Å [10]. Thus with the present combination of surface supercells, the lattice mismatch is only 1.3%. It is assumed that the

nanoparticles can adjust their structure to minimize surface stress.

The interface formation was modelled in two steps. First, the distance (Z) between the two slabs was numerically optimized starting from $Z = 10$ Å. The lattice parameters of this mixed structure were set to the average value of the two systems $a \equiv b = 13.0$ Å. In a second step the lattice parameter a was optimized taking the optimized value of Z . The optimized values of Z and a were 5.0 and 12.4 Å, corresponding to a substantial lateral contraction of 3–4%. In order to confirm that there was no introduction of artefacts due to the optimization procedure, we calculated the defect formation energy of Li A with a lattice constant of $a = 13.0$ Å (using equation (2)). Although the total energies of the defected and the stoichiometric reference model changed dramatically, the calculated defect formation energy only slightly increased from 486 to 489 kJ mol^{−1}.

Our model is infinite in two dimensions but non-periodic in the direction of the surface normal. The atoms in the uppermost and lowest layers are exposed to vacuum. We therefore divided the atomic layers into an interface region and an outer region. The interface region containing 75 atoms is marked with a box in figure 18(a).

It contains two Li layers and one O layer of the Li₂O surface and one B layer and two O layers of the B₂O₃ surface. The Li layer close to the B₂O₃ surface is denoted as the first layer, the other as the second layer. All atoms in the interface region are fully relaxed after optimization of the inter-layer distance Z and the lattice parameter a . The remaining atoms in the outermost layers are kept fixed at bulk-like positions in order to simulate the inner part of the nanoparticles. The final optimized structure is shown in figure 18(b).

To the best of our knowledge, this is the first atomistic model for the interface region between the ionic conductor and the insulator grains. Other metal–oxide interfaces and insulator–insulator oxide interfaces have been studied before with slab models at the DFT level and with classical force fields [138, 139].

In our model we assumed that (a) Li₂O and B₂O₃ nanoparticles have surfaces comparable to crystalline surfaces, and (b) stable contacts between the surfaces are more

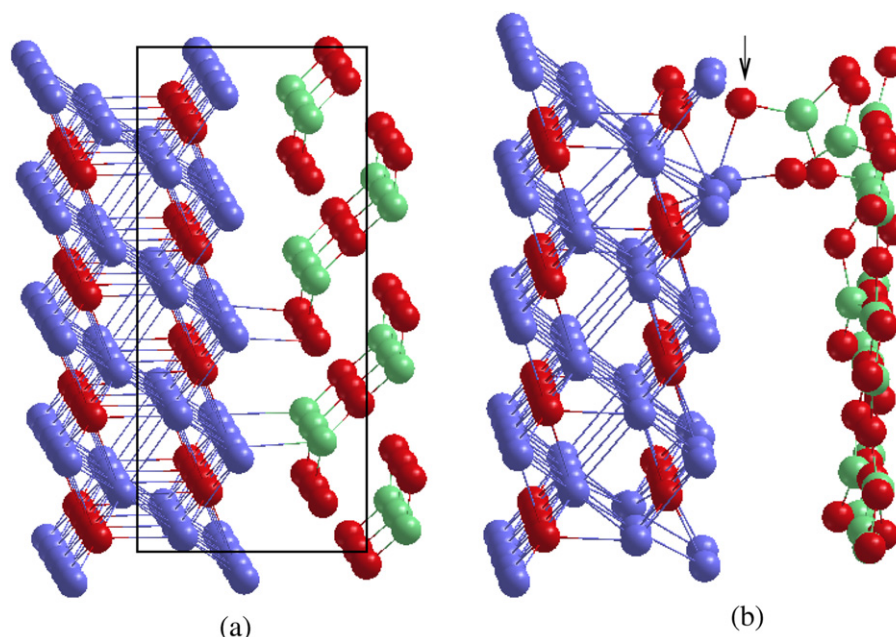


Figure 18. The interface of the $\text{Li}_2\text{O}:\text{B}_2\text{O}_3$ nanocomposite: (a) after the optimization of Z and a and (b) after optimization of the interface region taking the optimized Z and a . The blue, red and green spheres represent Li, O and B, respectively.

readily formed if their geometries are as similar as possible. The first assumption is justified by experimental studies of oxide nanoparticles demonstrating that even particles with only a few nanometre diameter have approximately bulk-like atomic structure [1]. In recent scanning tunnelling microscopy studies [140], it was shown that anatase nanoparticles have well-defined surface planes. Regarding the second assumption, there are of course many ways in which different surfaces of the two oxides can be combined. However, it is reasonable to assume that the selected building principle leads to a representative model of the nanocomposite system which is general enough to be applied in the present case and also for other combinations of oxides.

As a main result of the optimization, we observe the formation of a new boron–oxygen bond in the interface region. One of the oxygen atoms of the Li_2O surface (marked by an arrow in figure 18(b)) is pulled out of the surface layer towards a neighbouring boron atom of the B_2O_3 surface. Lithium atoms have two different types of coordination with oxygen atoms in the interface region. As a consequence of this dislocation, the coordination of a Li atom in the second layer is reduced from four to three (Li A in figure 19). The remaining four-fold coordinated Li atoms in the second layer are denoted as types D, E and F. The three-fold coordinated lithium atoms of the first layer (B, C and G in figure 19) do not change their coordination.

9.2. Defects

It is assumed that the reduced Li coordination and geometrical distortion due to the movement of the oxygen atom affects the energetics of defect formation in the interface region. This was investigated by calculating the lithium vacancy defect formation energy $E_{\text{de}}(\text{V})$ for types A–G, and the Frenkel

formation energy E_{Fr} for representative Li atoms (types A and B) in the interface region.

In table 21, the calculated values of $E_{\text{de}}(\text{V})$ and E_{Fr} for the $\text{Li}_2\text{O}:\text{B}_2\text{O}_3$ nanocomposite obtained with the PW1PW approach are compared with the PW1PW values for bulk Li_2O [10, 35] and the $\text{Li}_2\text{O}(111)$ surface [15] and also with available experimental data [34]. $E_{\text{de}}(\text{V})$ varies from 486 to 570 kJ mol^{-1} for the lithium types considered in the interface model. As expected, the defect formation energy for Li(A) with reduced coordination is the smallest (486 kJ mol^{-1}). Also the other three-fold coordinated lithium atoms B, C and G in the top layer have smaller defect formation energies (490, 498 and 531 kJ mol^{-1} , respectively) than the four-fold coordinated lithium atoms D, E and F in the second layer (550, 543 and 570 kJ mol^{-1} , respectively). Li(B) and Li(C) are closer to the dislocated oxygen than Li(G) and correspondingly their bond strengths are smaller.

For all the considered sites $E_{\text{de}}(\text{V})$ is smaller in the $\text{Li}_2\text{O}:\text{B}_2\text{O}_3$ interface than in the Li_2O bulk (580 kJ mol^{-1} , table 21), and smaller than in the corresponding lithium atoms (A1 and G1) in the $\text{Li}_2\text{O}(111)$ surface (543 and 498 kJ mol^{-1} respectively). A similar effect was observed for the Frenkel defect formation (table 21). E_{Fr} is much smaller in the $\text{Li}_2\text{O}:\text{B}_2\text{O}_3$ nanocomposite (113 kJ mol^{-1}) than in bulk Li_2O (216 kJ mol^{-1}). Our calculated bulk value is in agreement with experiment (244 kJ mol^{-1}) [34], and a previous (212 kJ mol^{-1}) DFT-LDA study [35]. As found for the vacancy formation, E_{Fr} in $\text{Li}_2\text{O}:\text{B}_2\text{O}_3$ nanocomposite is smaller than in the $\text{Li}_2\text{O}(111)$ surface (155 kJ mol^{-1}).

According to the defect formation energies, the interface region of $\text{Li}_2\text{O}:\text{B}_2\text{O}_3$ nanocomposites contains higher concentrations of both defect types than bulk Li_2O and the $\text{Li}_2\text{O}(111)$ surface. The similarity of the trends obtained for $E_{\text{de}}(\text{V})$ and E_{Fr} is not surprising since both defects involve

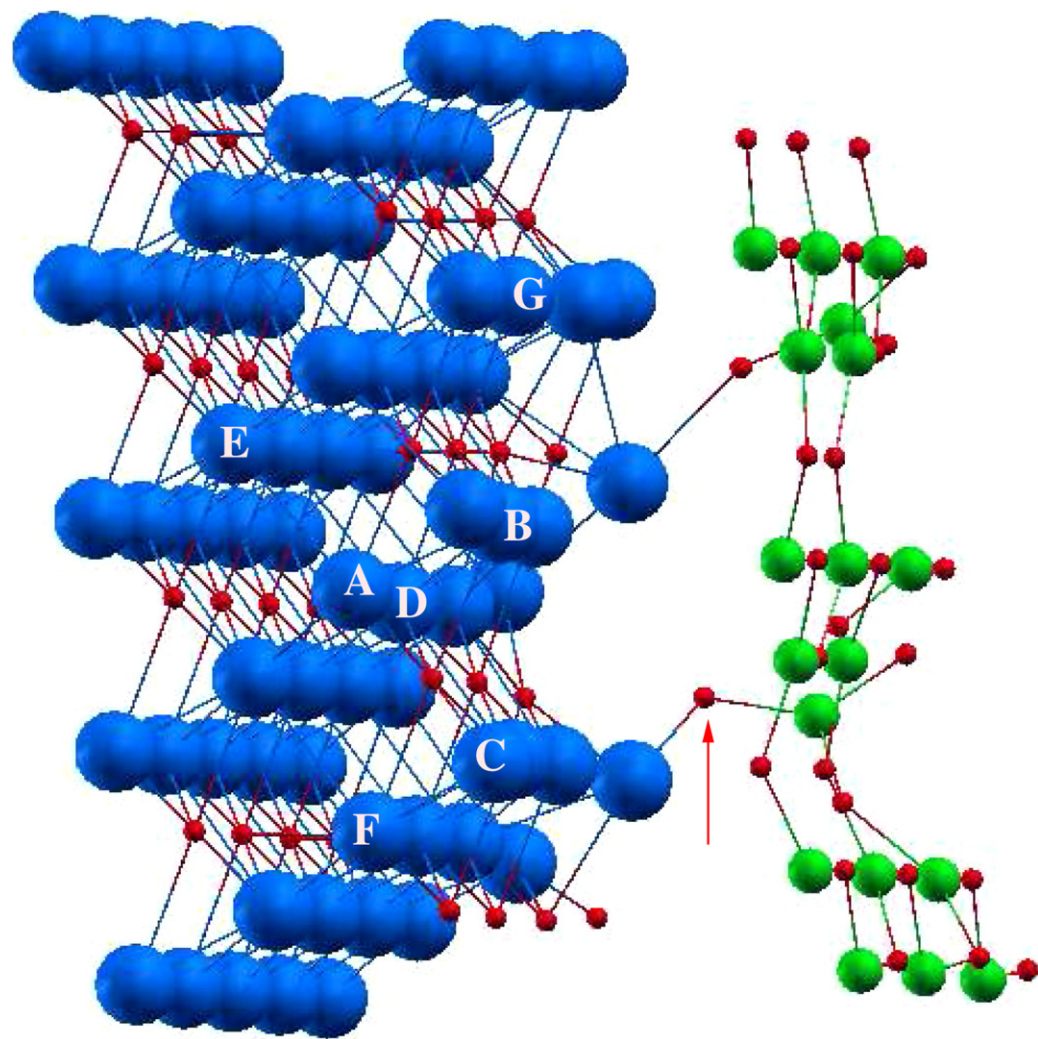


Figure 19. The interface of the $\text{Li}_2\text{O}:\text{B}_2\text{O}_3$ nanocomposite with the marked lithium atoms. The blue, red and green grey spheres represent Li, O and B, respectively.

Table 21. Calculated formation energies of a Li vacancy, $E_{\text{de}}(\text{V})$ (kJ mol^{-1}), and a Frenkel defect, E_{Fr} (kJ mol^{-1}), of $\text{Li}_2\text{O}:\text{B}_2\text{O}_3$ nanocomposite, crystalline Li_2O and a $\text{Li}_2\text{O}(111)$ surface (method: PW1PW) [9].

Li ₂ O:B ₂ O ₃								Li ₂ O		Li ₂ O(111) [15]	
Li	A	B	C	D	E	F	G	Calc.	Exp.	A1	G1
<i>E</i> _{de} (V)	486	490	498	550	543	570	531	580[10]		497	543
<i>E</i> _{Fr}	113							212 [35], 216 ^a	244 [34]	155	

^a This work.

the formation of an empty Li lattice site. Due to the different references, the absolute values of E_{Fr} are much smaller than those of $E_{\text{de}}(\text{V})$. The two defect types can be regarded as extreme cases of real lattice defects, where the dislocated Li is close to the vacancy (Frenkel defect) or at infinite distance (hole vacancy).

9.3. Li migration

In our theoretical investigation [9], we have performed calculations of activation barriers for hopping processes between regular lattice sites. As in the case of a $\text{Li}_2\text{O}(111)$

surface, Li migration may occur from a tetrahedral site to a cation vacancy which is three-fold coordinated to oxygen atoms, or vice versa. Another possibility is a hopping process between an occupied and an unoccupied three-fold coordinated site of the first layer. In both cases, one or two oxygen atoms are shared by the migrating Li^+ and the cation vacancy. Spin polarization plays an important role for the Li^+ migration. It was observed that the unpaired electron, created due to the cation vacancy, is localized on the 2p orbital of one of the surrounding oxygen atoms. The same situation was observed for the Li^+ diffusion in crystalline Li_2O [10, 15] and $\text{Li}_2\text{B}_4\text{O}_7$ [17].

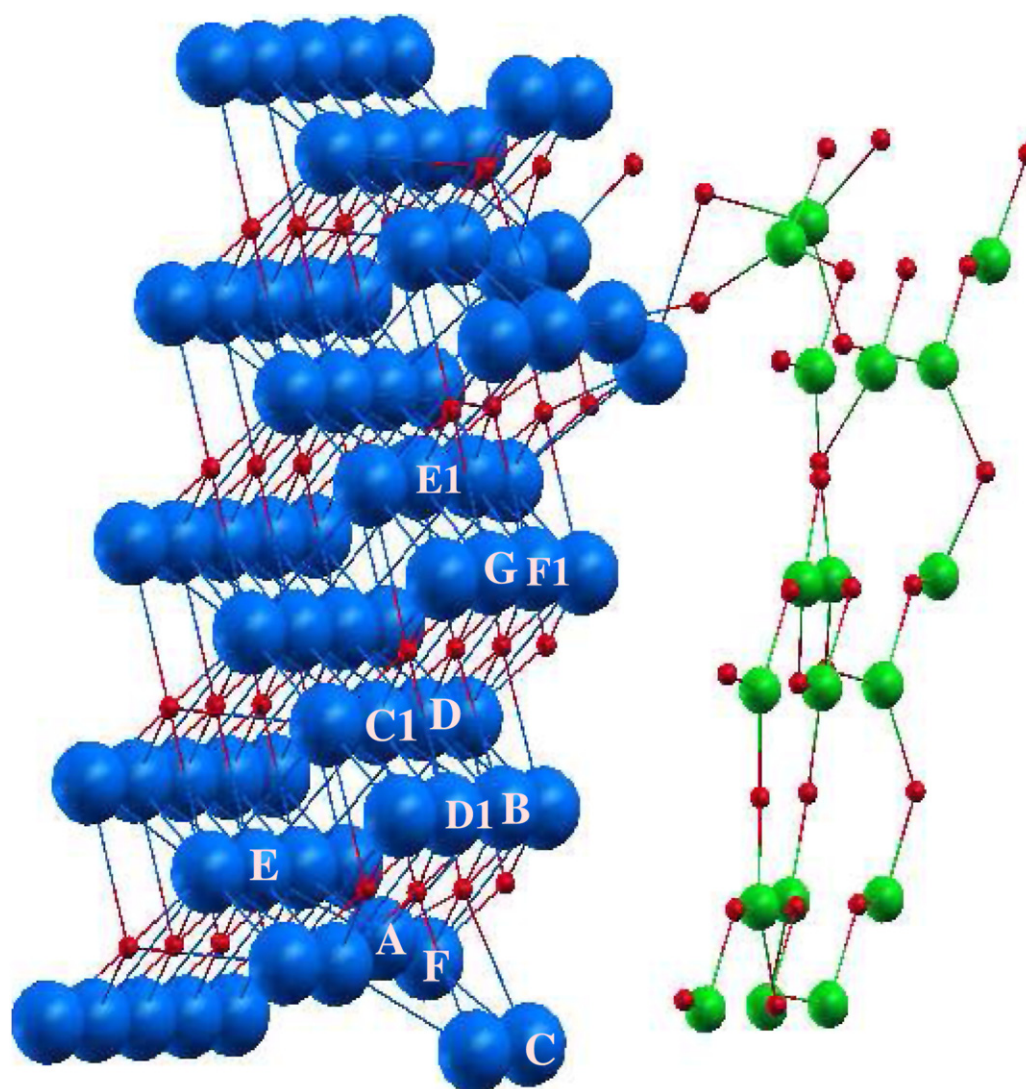


Figure 20. Possible pathways for Li^+ migration in the $\text{Li}_2\text{O}:\text{B}_2\text{O}_3$ interface.

In figure 20, selected lithium atoms are labelled to represent possible migration pathways for the Li^+ movement in the interface of $\text{Li}_2\text{O}:\text{B}_2\text{O}_3$ nanocomposite. As possible starting points, we selected two representative Li atoms, the second-layer Li(A) which becomes three-fold coordinated due to the dislocation of one oxygen, and the first-layer Li(G) which is at a large distance (6.45 \AA) from the dislocated oxygen. Migration of Li^+ can occur in a zig-zag pathway, via hopping from site $A \leftrightarrow B$, $A \leftrightarrow C$, $A \leftrightarrow E$, $G \leftrightarrow B$, $G \leftrightarrow C1$, or $G \leftrightarrow E1$. Alternatively, migration can occur straight along the x direction ($A \leftrightarrow D$ or $G \leftrightarrow D1$), or along the y direction ($A \leftrightarrow F$ or $G \leftrightarrow F1$).

The calculated values for the activation energy, E_A , for all considered possible migration pathways are presented in table 22.

Their smaller activation energies (0.1–1.2 eV) indicate that the zig-zag pathways are more suitable than the migrations along straight lines, along either the x direction ($E_A = 1.4\text{--}2.0 \text{ eV}$) or the y direction ($E_A = 1.7\text{--}2.7 \text{ eV}$). Several calculated values of E_A , e.g. for the processes $B \rightarrow A$

(0.10 eV) and $C1 \rightarrow G$ (0.22 eV), are much smaller than the experimental E_A of nanocrystalline Li_2O , 0.31 eV [1]. They are also smaller than the measured activation enthalpies in $\text{Li}_2\text{O}:\text{B}_2\text{O}_3$ nanocomposites ($0.34 \pm 0.04 \text{ eV}$ [3]) and in $\text{Li}_2\text{O}:\text{Al}_2\text{O}_3$ nanocomposites ($0.30 \pm 0.02 \text{ eV}$ [6]). However, it has to be taken into account that in these experiments an average over the manifold of local hopping processes is obtained. Since the measurements have been performed at 300–500 K, it can be assumed that activation energies larger than 1 eV cannot be overcome in the time scale of NMR experiments. This excludes all straight pathways and also some of the zig-zag pathways. The average of the remaining nine calculated activation energies is 0.28 eV, in close agreement with the reported experimental values.

10. Summary and conclusions

The energetics, structural relaxation, electronic properties, defect properties and ionic diffusion of $(\text{Li}_2\text{O})_x(\text{B}_2\text{O}_3)_{1-x}$ ($x = 0.33, 0.5$ and 1.0) compounds and at the interfaces

Table 22. Comparison of calculated activation energies, E_A (eV), for Li hopping in $\text{Li}_2\text{O}:\text{B}_2\text{O}_3$ nanocomposite and bulk Li_2O with experimental data [9].

	$\text{Li}_2\text{O}:\text{B}_2\text{O}_3$										Li_2O		$\text{Li}_2\text{O}:\text{Al}_2\text{O}_3$
	Calc.										Calc.	Exp. [1]	Exp. [6]
	A (second layer close to dislocated O)					G (first layer far from dislocated O)							
<i>a</i>	B	C	D	E	F	B	C1	D1	E1	F1			
$E_A(ab)$	0.10	1.08	2.04	0.56	2.72	1.18	0.22	2.00	0.39	1.88	0.34 ± 0.04	0.33 [10] (0.34 [35])	0.30 ± 0.02
$E_A(ba)$	0.09	0.68	1.37	0.29	1.68	1.06	0.05	1.97	0.18	1.80			

of $\text{Li}_2\text{O}:\text{B}_2\text{O}_3$ nanocomposite were investigated theoretically. The reliability of four quantum-chemical approaches was tested for the above mentioned properties by comparison of calculated and available experimental data. For all the systems under consideration, the hybrid PW1PW method gives the best agreement with experiment among the considered methods. The effect of different kinds of basis sets, atom-centred and delocalized plane waves, on the results obtained with the same density-functional method, PWGGA, was studied systematically. The basis set dependence of the geometry parameters is small, but is more pronounced for electronic properties. The investigation of basis set dependence of the LCAO based approaches was performed by augmentation of the Li, B and O basis sets. It was found that the addition of polarization and diffuse basis functions to Li and B atoms leads to a significant improvement of the calculated electronic spectra, while the effect on structure parameters and energetics is small.

All $(\text{Li}_2\text{O})_x(\text{B}_2\text{O}_3)_{1-x}$ ($x = 0.33, 0.5$ and 1.0) compounds are large gap insulators with calculated band gaps of 7.95 eV for Li_2O , 8.80 eV for B_2O_3 , 8.19 eV for LiBO_2 and 9.31 eV for $\text{Li}_2\text{B}_4\text{O}_7$ obtained with the PW1PW method. Comparison of available experimental data shows that the deviation of the calculated bandgaps from experiment is less than 1.0%. The deviations of the calculated structural properties and energetics from the experiment are less than 1.5% and 0.5% respectively with this method. The comparison of two proposed structures, $P3_121$ and $P3_1$, of crystalline B_2O_3 shows that the structure with $P3_121$ space group symmetry is the global minimum.

In accordance with previous quantum-chemical studies, it was found that the (111) surface is thermodynamically the most stable surface of Li_2O . Surface relaxation is more pronounced for the (110) surface compared to the (111) surface. The bandgaps for both surfaces are reduced with respect to the bulk due to the presence of surface excitons. By comparing the structures and energetics of some selected low-index surfaces ((101), $(1\bar{1}1)$, (100) and (001)) of B_2O_3 , we conclude that the most stable surface is (101). The surfaces have occupied surface states slightly above the VB top, even for the optimized (101) surface where no dangling bonds are present.

Defect properties were investigated by calculating the defect formation energy, structural relaxation and electronic properties such as DOSs for the defective supercells. It was observed that the relaxation around the cation vacancy is

mainly restricted to the first- and second-nearest-neighbour atoms for all the systems, which is not surprising taking into account the ionic nature of the Li–oxygen bond. The analysis of electronic properties showed that the Li^+ ion vacancy introduces an extra unoccupied level below the bottom of the conduction band. The structural relaxation around the F centre in Li_2O is rather short-ranged. It is restricted to the first-nearest-neighbour atoms. The removal of a neutral oxygen leads to the formation of a doubly occupied defect level above the valence band.

The comparison of an isolated cation vacancy and a cation Frenkel defect in the bulk and in the most stable (111) surface of Li_2O was performed. The calculated defect formation energy for the Li_2O surface (539 kJ mol^{-1}) is significantly smaller than the corresponding value for the bulk (576 kJ mol^{-1}). The effect is even more pronounced for the cation Frenkel formation energy, which is 151 kJ mol^{-1} for the (111) surface and 244 kJ mol^{-1} for the bulk. We therefore conclude that the defect concentration in the (111) surface is larger than in the bulk.

The ion conductivities of the Li_2O bulk and (111) surface, LiBO_2 bulk and $\text{Li}_2\text{B}_4\text{O}_7$ bulk were investigated by calculating the activation energies (E_A) for local hopping processes. Our calculated E_A values of 0.33 eV (Li_2O bulk), 0.25 eV ($\text{Li}_2\text{O}(111)$ surface), 0.43–0.55 eV (LiBO_2 bulk) and 0.37 eV ($\text{Li}_2\text{B}_4\text{O}_7$ bulk) are in good agreement with the experimental data. Our investigation reveals various different local hopping mechanisms for all the considered systems. In Li_2O bulk, the migration of a Li^+ ion occurs in an almost straight line, whereas in the surfaces of Li_2O , the most likely mechanism for Li^+ migration is in a zig-zag pathway rather than in a straight line along a direction parallel to the surface plane. In LiBO_2 , Li^+ ion migration can occur along the c direction and in the xy plane, with a slight preference for Li diffusion in the plane. In $\text{Li}_2\text{B}_4\text{O}_7$, the Li^+ migrates through a one-dimensional channel of five-vertex oxygen polyhedra along the tetragonal axis.

On the basis of all these theoretical studies, we have developed an atomistic model of nanocrystalline $\text{Li}_2\text{O}:\text{B}_2\text{O}_3$ composites. It was found that the Li–O bonds are weakened and simultaneously B–O bonds are formed at the boundary between the two surfaces. This preference for oxygen bonding with B (or Al in $\text{Li}_2\text{O}:\text{Al}_2\text{O}_3$) plays a key role in generating low-coordinated Li. The removal of surface oxygen from Li_2O is responsible for the increased vacancy defect concentration in $\text{Li}_2\text{O}:\text{B}_2\text{O}_3$ (or $\text{Li}_2\text{O}:\text{Al}_2\text{O}_3$)

nanocomposite materials. We propose that nanocomposites of ionic compounds (containing weakly bound and therefore mobile cations) with highly covalent compounds (with strong metal– or nonmetal–oxygen bonds) are in general promising candidates for high ionic conductivity.

Our model calculations show that the most likely mechanism for Li^+ migration is in a zig-zag pathway rather than in a straight line along a direction parallel to the interface plane, as in the case of Li_2O bare surfaces. The averaged calculated activation energy for Li^+ migration in the $\text{Li}_2\text{O}:\text{B}_2\text{O}_3$ interface is similar to the experimental values for bulk Li_2O and $\text{Li}_2\text{O}:\text{B}_2\text{O}_3$ and $\text{Li}_2\text{O}:\text{Al}_2\text{O}_3$ nanocomposites. We therefore conclude that the experimentally observed enhanced Li mobility in the $\text{Li}_2\text{O}:\text{B}_2\text{O}_3$ interface region is thermodynamically and not kinetically controlled.

Acknowledgments

This work was supported by the State of Lower Saxony, Germany, in the framework of a ‘Georg Christoph Lichtenberg’ fellowship (M M Islam). We also thank the Deutsche Forschungsgemeinschaft (DFG) for the funding of DFG-Forschergruppe 1277 molife (Mobilität von Li-Ionen in Festkörpern).

References

- [1] Heitjans P and Indris S 2003 *J. Phys.: Condens. Matter* **15** R1257–89
- [2] Indris S, Heitjans P, Roman H E and Bunde A 2000 *Phys. Rev. Lett.* **84** 2889–92
- [3] Indris S and Heitjans P 2002 *J. Non-Cryst. Solids* **307–310** 555–64
- [4] Ulrich M, Bunde A, Indris S and Heitjans P 2004 *Phys. Chem. Chem. Phys.* **6** 3680–3
- [5] Indris S, Heitjans P, Ulrich M and Bunde A 2005 *Z. Phys. Chem.* **219** 89–103
- [6] Wilkening M, Indris S and Heitjans P 2003 *Phys. Chem. Chem. Phys.* **5** 2225–31
- [7] Knauth P 2000 *J. Electroceram.* **5** 111–25
- [8] Maier J 2004 *Physical Chemistry of Ionic Materials* (West Sussex: Wiley)
- [9] Islam M M, Bredow T, Indris S and Heitjans P 2007 *Phys. Rev. Lett.* **99** 1455021
- [10] Islam M M, Bredow T and Minot C 2006 *J. Phys. Chem. B* **110** 9413–20
- [11] Islam M M, Bredow T and Minot C 2006 *Chem. Phys. Lett.* **418** 565–8
- [12] Islam M M, Bredow T and Heitjans P 2011 *J. Phys. Chem. C* **115** 12343–9
- [13] Maslyuk V V, Islam M M and Bredow T 2005 *Phys. Rev. B* **72** 1251011
- [14] Islam M M, Maslyuk V V, Bredow T and Minot C 2005 *J. Phys. Chem. B* **109** 13597–604
- [15] Islam M M and Bredow T 2009 *J. Phys. Chem. C* **113** 672–6
- [16] Bredow T and Islam M M 2008 *Surf. Sci.* **602** 2217–21
- [17] Islam M M, Bredow T and Minot C 2006 *J. Phys. Chem. B* **110** 17518–23
- [18] Keen D A 2002 *J. Phys.: Condens. Matter* **14** R819–57
- [19] Noda K, Ishii Y, Ohno H, Watanabe H and Matsui H 1989 *Adv. Ceram. Mater.* **25** 155
- [20] Johnson C E, Kummerer K R and Roth E 1988 *J. Nucl. Mater.* **155–157** 188–201
- [21] Dovesi R, Roetti C, Freyria-Fava C, Prencipe M and Saunders V R 1991 *Chem. Phys.* **156** 11–9
- [22] Shukla A, Dolg M, Fulde P and Stoll H 1998 *J. Chem. Phys.* **108** 8521–7
- [23] Dovesi R 1985 *Solid State Commun.* **54** 183–5
- [24] Mikajlo E A, Nixon K L, Coleman V A and Ford M J 2002 *J. Phys.: Condens. Matter* **14** 3587–98
- [25] Liu L, Henrich V E, Ellis W P and Shindo I 1996 *Phys. Rev. B* **54** 2236–9
- [26] Albrecht S, Onida G and Reining L 1997 *Phys. Rev. B* **55** 10278–81
- [27] Hull S, Farley T W D, Hayes W and Hutchings M T 1988 *J. Nucl. Mater.* **160** 125–34
- [28] Rauch W 1940 *Z. Phys.* **116** 652–6
- [29] Itoh M, Murakami J and Ishii Y 1999 *Phys. Status Solidi b* **213** 243–51
- [30] Masaki N M, Noda K, Watanabe H, Clemmer R G and Hollenberg G W 1994 *J. Nucl. Mater.* **212–215** 908–11
- [31] Noda K, Ishii Y, Matsui H and Watanabe H 1985 *J. Nucl. Mater.* **133/134** 205–8
- [32] Ishii Y, Murakami J and Itoh M 1999 *J. Phys. Soc. Japan* **68** 696–7
- [33] De Vita A, Manassidis I, Lin J S and Gillan M J 1992 *Europhys. Lett.* **19** 605–10
- [34] Chadwick A V, Flack K W, Strange J H and Harding J 1988 *Solid State Ion.* **28–30** 185–8
- [35] De Vita A, Gillan M J, Lin J S, Payne M C, Stich I and Clarke L J 1992 *Phys. Rev. Lett.* **68** 3319–22
- [36] Shluger A and Itoh N 1990 *J. Phys.: Condens. Matter* **2** 4119
- [37] Tanigawa H and Tanaka S 2002 *J. Nucl. Mater.* **307–311** 1446–50
- [38] Noda K, Ishii Y, Matsui H and Watanabe H 1986 *Radiat. Eff.* **97** 297–305
- [39] Baker J M, Cox A, O’Connell A J and Ward R C C 1991 *J. Phys.: Condens. Matter* **3** 6189–93
- [40] Mackrodt W C 1988 *J. Mol. Liq.* **39** 121–36
- [41] Noda K, Uchida K, Tanifuji T and Nasu S 1980 *J. Nucl. Mater.* **91** 234–6
- [42] Noda K, Uchida K, Tanifuji T and Nasu S 1981 *Phys. Rev. B* **24** 3736–42
- [43] Koyama Y, Yamada Y, Tanaka I, Nishitani S R, Adachi H, Murayama M and Kanno R 2002 *Mater. Trans.* **43** 1460–3
- [44] Hayoun M, Meyer M and Denieport A 2005 *Acta Mater.* **53** 2867–74
- [45] Pfeiffer H, Sánchez-Sánchez J and Álvarez L J 2000 *J. Nucl. Mater.* **280** 295–303
- [46] Goel P, Choudhury N and Chaplot S L 2004 *Phys. Rev. B* **70** 174307
- [47] Fracchia R M, Barrera G D, Allan N L, Barron T H K and Mackrodt W C 1998 *J. Phys. Chem. Solids* **59** 435–45
- [48] Chawla N, Kerr M and Chawla K K 2005 *J. Am. Ceram. Soc.* **88** 101–8
- [49] Effenberger H, Lengauer C L and Parthe E 2001 *Monatsh. Chem.* **132** 1515–7
- [50] Gurr G E, Montgomery P W, Knutson C D and Gorres B T 1970 *Acta Crystallogr. B* **26** 906–15
- [51] Prewitt C T and Shannon R D 1968 *Acta Crystallogr. B* **24** 869–74
- [52] 1991–1992 *CRC Handbook of Chemistry and Physics* 72nd edn (Boca Raton, FL: CRC Press)
- [53] Ong C W, Huang H, Zheng B, Kwok R W M, Hui Y Y and Lau W M 2004 *J. Appl. Phys.* **95** 3527–34
- [54] Muramatsu Y, Takenaka H, Oyama T, Hayashi T, Grush M M and Perera R C C 1999 *X-Ray Spectrom.* **28** 503–8
- [55] Li D and Ching W Y 1996 *Phys. Rev. B* **54** 13616–22
- [56] Takada A, Catlow C R A, Price G D and Hayward C L 1997 *Phys. Chem. Miner.* **24** 423–31

- [57] Sastry B S R and Hummel F A 1958 *J. Am. Ceram. Soc.* **41** 7–17
- [58] Sastry B S R and Hummel F A 1959 *J. Am. Ceram. Soc.* **42** 216–8
- [59] Aver'yanov V I and Kalmykov A E 1990 *Glass Phys. Chem.* **16** 492–4
- [60] Jiang A, Lei S, Huang O, Chen T and Ke D 1990 *Acta Crystallogr. C* **46** 1999–2001
- [61] Liu H, Shen G, Wang X, Wei J and Shen D 2000 *Prog. Cryst. Growth Charact.* **40** 235–41
- [62] Huang C, Wang S and Ye N 2010 *J. Alloys Compounds* **502** 211–4
- [63] Ingamells C O 1970 *Anal. Chim. Acta* **52** 323
- [64] He K, He D, Lei L, Zou Y, Qin J and Wang S 2010 *Solid State Commun.* **150** 2106–8
- [65] Motabar P, Inn K G W, Davis J and LaRosa J 2009 *J. Radioanal. Nucl. Chem.* **282** 335–41
- [66] Smith R W and Keszler D A 1991 *J. Solid State Chem.* **93** 430
- [67] Moshopoulou E G 1999 *J. Am. Ceram. Soc.* **82** 3317–20
- [68] Kageyama H, Onizuka K, Yamauchi T and Ueda Y 1999 *J. Cryst. Growth* **206** 65–7
- [69] Santos M C, Nogueira A R A and Nóbrega J A 2005 *J. Braz. Chem. Soc.* **16** 372–80
- [70] Becker P 1998 *Adv. Mater.* **10** 979–92
- [71] Mcmillen C D, Giesber H G and Kolis J W 2008 *J. Cryst. Growth* **310** 299–305
- [72] Heitjans P, Tobschall E and Wilkening M 2008 *Eur. Phys. J.* **161** 97–108
- [73] Kuhn A, Tobschall E and Heitjans P 2009 *Z. Phys. Chem.* **223** 1359–77
- [74] Gardner D 2009 *Renew. Energy Focus* **9** 34–7
- [75] Conte M, Iacobazzi A, Ronchetti M and Vellone R 2001 *J. Power Sources* **100** 171–87
- [76] Goudon J P, Bernard F, Renouard J and Yvart P 2010 *Int. J. Hydrog. Energy* **35** 11071–6
- [77] Komatsu R, Sugawara T and Watanabe N 1999 *Rev. Laser Eng.* **27** 541–6
- [78] Jung H-R, Jin B-M, Cha J-W and Kim J-N 1997 *Mater. Lett.* **30** 41–5
- [79] Otsuka K, Funami M, Ito M, Katsuda H, Tacano M, Adachi I M and Kawabata A 1995 *Japan. J. Appl. Phys.* **34** 2646–9
- [80] Takeuchi M, Odagawa I, Tanaka M and Yamanouchi K 1997 *Japan. J. Appl. Phys.* **36** 3091–5
- [81] Shestopalov K V, Nefedov V A and Zadneprovsky B I 1994 *Proc. 1994 IEEE Int. Frequency Control Symp.* vol 301 (Boston)
- [82] Whatmore R W, Shorrocks N M, O'Hara C, Ainger F W and Young I M 1981 *Electron. Lett.* **17** 11–2
- [83] Komatsu R, Sugawara T, Sassa K, Sarukura N, Liu Z, Izumida S, Segawa Y, Uda S, Fukuda T and Yamanouchi K 1997 *Appl. Phys. Lett.* **70** 3492–4
- [84] Sugawara T, Komatsu R and Uda S 1998 *Solid State Commun.* **107** 233–7
- [85] Adachi M, Nakazawa K and Kawabata A 1997 *Ferroelectrics* **195** 123–6
- [86] Filipiak J, Majchrowski A and Lukasiewicz T 1994 *Arch. Acoust.* **19** 131
- [87] Bhalla A S, Cross L E and Whatmore R W 1985 *Japan. J. Appl. Phys.* **24** (Suppl. 24/2) 727–9
- [88] Ono M, Sakai M, Fujiwara Y and Wakatsuki N 1997 *Proc. 1997 IEEE Ultrasonics Symp.* vol 2, (Toronto) p 1047
- [89] Furetta C and Weng P S 1998 *Operation Thermoluminescent Dosimetry* (London: World Scientific)
- [90] Mahesh K, Weng P S and Furetta C 1989 *Thermoluminescence in Solids and Its Applications* (Ashford: Nuclear Technology Publishing)
- [91] Dolzhenkova E F, Baumer V N, Tolmachev A V, Hunda B M and Puga P P 2001 *6th Int. Conf. on Inorganic Scintillators and Their Applications* vol 210 (Chamonix, France)
- [92] Kim C-S, Park J-H, Moon B K, Seo H-J, Choi B-Ch, Hwang Y-H, Kim H K and Kim J N 2003 *J. Appl. Phys.* **94** 7246–9
- [93] Kim C-S, Kim D J, Hwang Y-H, Kim H K and Kim J N 2002 *J. Appl. Phys.* **92** 4644–8
- [94] Rizak I M, Rizak V M, Baisa N D, Bilanich V S, Boguslavskii M V, Stefanovich S Yu and Golovei V M 2003 *Crystallogr. Rep.* **48** 676–81
- [95] Rizak V M, Rizak I M, Bausa N D, Bilanych V S, Stefanovich S Yu, Bohuslavskii M B and Holovey V M 2003 *Ferroelectrics* **286** 49–59
- [96] Kim C-S, Hwang Y H, Kim H K and Kim J N 2003 *Phys. Chem. Glasses* **44** 166–9
- [97] Button D P, Mason L S, Tuller H L and Uhlmann D R 1983 *Solid State Ion.* **9/10** 585–92
- [98] Paul G L and Taylor W 1982 *J. Phys. C* **15** 1753–64
- [99] Ogorodnikov I N, Pustovarov V A, Kurzhalov A V, Isaenko L I, Kirm M and Zimmerer G 2000 *Phys. Solid State* **42** 464–72
- [100] Kuznetsov A Y, Kruzhalov A V, Ogorodnikov I N, Sobolev A B and Isaenko L I 1999 *Phys. Solid State* **41** 48–50
- [101] Burak Ya V, Dovgii Ya O and Kityk I V 1989 *Sov. Phys.—Solid State* **31** 1634
- [102] Perdew J P and Wang Y 1992 *Phys. Rev. B* **45** 13244–9
- [103] Perdew J P, Chevary J A, Vosko S H, Jackson K A, Penderson M R, Singh D J and Fiolhais C 1992 *Phys. Rev. B* **46** 6671–87
- [104] Bredow T and Gerson A R 2000 *Phys. Rev. B* **61** 5194–201
- [105] Becke A D 1993 *J. Chem. Phys.* **98** 5648–52
- [106] Lee C, Yang W and Parr R G 1988 *Phys. Rev. B* **37** 785–9
- [107] Dovesi R, Saunders V R, Roetti C, Orlando R, Zicovich-Wilson C M, Pascale F, Civalieri B, Doll K, Harrison N M, Bush I J, D'Arco P and Llunell M 2009 *CRYSTAL09 CRYSTAL09 Users Manual* (Torino: University of Torino)
- [108] Prencipe M, Zupan A, Dovesi R, Aprà E and Saunders V R 1995 *Phys. Rev. B* **51** 3391–6
- [109] Ojamäe L, Hermansson K, Pisani C, Causà M and Roetti C 1994 *Acta Crystallogr. B* **50** 268–79
- [110] Bredow T, Heitjans P and Wilkening M 2004 *Phys. Rev. B* **70** 115111
- [111] Orlando R, Dovesi R and Roetti C 1990 *J. Phys.: Condens. Matter* **2** 7769–89
- [112] Catti M, Valerio G, Dovesi R and Causà M 1994 *Phys. Rev. B* **49** 14179–87
- [113] Kresse G and Hafner J 1993 *Phys. Rev. B* **47** 558–61
- [114] Kresse G and Hafner J 1993 *Phys. Rev. B* **48** 13115–8
- [115] Kresse G and Hafner J 1994 *Phys. Rev. B* **49** 14251–69
- [116] Kresse G and Joubert J 1999 *Phys. Rev. B* **59** 1758–75
- [117] Blöchl P E 1994 *Phys. Rev. B* **50** 17953–79
- [118] VASP guide <http://cms.mpi.univie.ac.at/vasp/vasp/vasp.html>
- [119] Wyckoff R 1963 *Crystal Structures* (New York: Interscience)
- [120] Monkhorst H J and Pack J D 1976 *Phys. Rev.* **13** 5188–92
- [121] Kovalev O V 1993 *Representations of the Crystallographic Space Groups: Irreducible Representations, Induced Representations, and Corepresentations* (Philadelphia, PA: Gordon and Breach)
- [122] Fuentealba P, Preuss H, Stoll H and Szentpaly L V 1982 *Chem. Phys. Lett.* **89** 418–22
- [123] Igel-Mann G, Stoll H and Preuss H 1988 *Mol. Phys.* **65** 1321–8
- [124] Kirfel A, Will G and Stewart R F 1983 *Acta Crystallogr. B* **39** 175–85
- [125] Kubaschewski O, Alock C B and Spencer P J 1992 *Materials Thermochemistry* 6th edn (New York: Pergamon) p 288

- [126] Xu Y-N and Ching W Y 1990 *Phys. Rev. B* **41** 5471–4
- [127] Pisani C, Dovesi R and Roetti C 1988 *Hartree-ock Ab Initio Treatment of Crystalline Systems (Lecture Notes in Chemistry vol 48)* (Heidelberg: Springer)
- [128] Radaev S V, Muradyan L A, Malakhova L F, Burak Y V and Simonov V I 1989 *Kristallografiya* **34** 1400
- [129] Hsu W Y and Kasowski R V 1993 *J. Appl. Phys.* **73** 4101–3
- [130] Mackrodt W C and Tasker P W 1985 *Chem. Br.* **21** 366–9
- [131] Lichanot A, Gelize M, Larrieu C and Pisani C 1991 *J. Phys. Chem. Solids* **52** 1155–64
- [132] Lazzeri M, Vittadini A and Selloni A 2001 *Phys. Rev. B* **63** 155409
- Lazzeri M, Vittadini A and Selloni A 2002 *Phys. Rev. B* **65** 119901
- [133] Evarestov R A, Bredow T and Jug K 2001 *Phys. Solid State* **43** 1774–82
- [134] Karan N K, Natesan B and Katiyar R S 2006 *Solid State Ion.* **177** 1429–36
- [135] Aliev A É, Burak V Ya and Lyseiko I T 1990 *Izv. Akad. Nauk SSSR Neorg. Mater.* **26** 1991
- [136] Burak A V, Lyseiko I T and Garapin I V 1989 *Ukr. Fiz. Zh.* **34** 226–8
- [137] Krogh-Moe J 1968 *Acta. Crystallogr. B* **24** 179–81
- [138] Catlow C R A, French S A, Sokol A A, Alfredsson M and Bromley S T 2003 *Faraday Discuss.* **124** 185–203
- [139] Sayle D C, Catlow C R A, Harding J H, Healy M J F, Maicaneanu S A, Parker S C, Slater B and Watson W G 2000 *J. Mater. Chem.* **10** 1315–24
- [140] Feldhoff A, Mendive C, Bredow T and Bahnemann D 2007 *Chem. Phys. Chem.* **8** 805–9
- [141] Yungman V S (ed) 1999 *Thermal Constants of Substances* vol 4 (New York: Wiley)